

CHALMERS



Doping dependent transport in YBCO nanostructures: insights into the microscopic mechanism for high critical temperature superconductivity

Thesis for the Degree of Erasmus Mundus Master of Nanoscience and Nanotechnology

RANKO TOSKOVIC

Promoter:

Professor Floriana Lombardi, *Chalmers University of Technology*

Co-Promoter:

Associate Professor Frederik Deneff, *KU Leuven*

External Referee:

Professor Göran Johansson, *Chalmers University of Technology*

Department of Microtechnology and Nanoscience

CHALMERS UNIVERSITY OF TECHNOLOGY

Göteborg, Sweden 2013



KU LEUVEN

THESIS FOR THE DEGREE
OF
ERASMUS MUNDUS MASTER OF NANOSCIENCE AND NANOTECHNOLOGY

Doping dependent transport in YBCO
nanostructures: insights into the
microscopic mechanism for high critical
temperature superconductivity

RANKO TOSKOVIC

This thesis was carried out as a part of the Erasmus Mundus Master program of
Nanoscience and Nanotechnology with the trajectory Nanophysics
KU Leuven - Chalmers University of Technology

Department of Microtechnology and Nanoscience
CHALMERS UNIVERSITY OF TECHNOLOGY
Göteborg, Sweden 2013

Doping dependent transport in YBCO nanostructures: insights into the microscopic mechanism for high critical temperature superconductivity

Ranko Toskovic

Thesis for the Degree of Erasmus Mundus Master of Nanoscience and Nanotechnology

© Ranko Toskovic, 2013

Quantum Device Physics Laboratory
Department of Microtechnology and Nanoscience
CHALMERS UNIVERSITY OF TECHNOLOGY
SE-412 96 Göteborg
Sweden
www.chalmers.se
Tel. +46-(0)31 772 1000

Cover:

Printed by Chalmers Reproservice
Göteborg, Sweden 2013

Abstract

The microscopic mechanism responsible for superconductivity in high critical temperature superconductors (HTSs), almost three decades after their discovery, still remains unknown. It is widely believed that studies in the underdoped (UD) regime of these materials could shed light on this unresolved question.

In this thesis project, a controllable and reproducible Pulsed Laser Deposition (PLD) growth of underdoped $\text{YBa}_2\text{Cu}_3\text{O}_{7-\delta}$ (YBCO) films was done by changing only the post-annealing pressure. X ray diffractometry (XRD) $2\theta - \omega$ scans of the films have shown a continuous YBCO unit cell expansion as the pressure decreased, indicating a reduction in the doping level of our films. Rather sharp resistance vs. temperature transitions obtained in our films indicate a high level of homogeneity. First steps towards optimization of the surface properties of the films have been also undertaken.

A soft-patterning technique developed previously in our group, preserving homogeneity of submicron structures, was employed for nanorings' patterning on the optimally doped films. Little Parks (LP) experiments were conducted on rings with different sizes. Cooper pairs have been identified as the predominant charge carriers in all the rings, as expected at the optimal doping level.

Keywords: high critical temperature superconductivity, YBCO, Little Parks effect, underdoped and optimally doped films, nanorings

Symbols

T_c	Critical temperature
δ	Oxygen doping parameter
p_{pa}	Post-annealing pressure
T_d	Deposition temperature
ΔT_c	Critical temperature oscillations amplitude
T_{onset}	Onset temperature of the resistive transition
ΔT	Resistive transition width

v_s	Superfluid velocity
R	Resistance
B	Magnetic inductance
Φ	Magnetic flux
Φ'	Magnetic fluxoid
Φ_0	Magnetic flux quanta
r	Radius of the loop enclosing Φ_0
w	Arm width of the ring
d_{in}	Inner diameter of the ring
ξ_0	Zero-temperature coherence length

Abbreviations

LTS	Low critical Temperature Superconductor
HTS	High critical Temperature Superconductor
YBCO	Yttrium Barium Copper Oxide
SC	Superconducting
OP	Order Parameter
BCS	Bardeen-Cooper-Schrieffer
UD	Underdoped
LAO	Lanthanum Aluminum Oxide
PLD	Pulsed Laser Deposition
XRD	X-Ray Diffractometry
PPMS	Physical Properties Measurements System
SEM	Scanning Electron Microscopy

AFM	Atomic Force Microscopy
MC	Multiply Connected
LP	Little Parks
MR	Magnetoresistance
FFT	Fast Fourier Transform

Contents

1	Introduction	1
1.1	Motivation.....	1
1.2	Theoretical background.....	3
1.2.1	Conventional vs. high critical temperature superconductivity.....	3
1.2.2	YBCO – structure, phase diagram and superconducting properties.....	4
1.2.3	Little Parks effect.....	8
2	Deposition and characterization of YBCO films	13
2.1	The substrate choice.....	13
2.2	Doping dependent YBCO films.....	14
2.2.1	Pulsed Laser Deposition.....	15
2.2.2	Characterization of YBCO films.....	17
2.2.2.1	Electronic properties.....	17
2.2.2.2	Crystallographic properties.....	21
2.2.2.3	Surface properties.....	24
3	Fabrication of optimally doped YBCO nanorings	27
4	Transport measurements	31
5	Conclusions and future outlook	41
	Appendix A – XRD	43
	Appendix B - PPMS	45
	Acknowledgements	47
	Bibliography	49

Chapter 1

Introduction

1.1 Motivation

Since their discovery in 1986 [1], high- T_c superconductors (HTSs) have attracted great attention due to their rather high critical temperature (T_c) and ability to sustain large currents and magnetic fields while preserving the superconducting (SC) state, which can be highly useful for applications. Some knowledge on the symmetry of the order parameter (OP) has been collected [2]-[7]. It is well established by now that the dominant component of the OP in HTSs is of $d_{x^2-y^2}$ type. The microscopic theory providing explanation on the origin of superconductivity in these materials is still missing.

The interplay between several degrees of freedom in these systems (charge, spin, orbit, lattice) requires further addressing for formulating the microscopic theory for HTSs. Two different streams have been followed in the attempts to provide an explanation. Some propose models which include phonon assistance in the formation of SC charge carriers, whilst reminding that if that is actually the case, the mechanism has to be more complex than the one proposed in the Bardeen-Cooper-Schrieffer (BCS) theory [8]. Others suggest models that include spin-spin interaction rather than the electron-phonon one [9]. In addition, the normal state of these materials introduces a peculiar behavior described by the existence of a gap in the electronic density of states in the underdoped (UD) regime¹ at temperatures higher than the critical one in the corresponding direction of the k space where the $d_{x^2-y^2}$ order parameter has its maximum [10]

¹ More on different parts of the SC phase diagram can be found in section 1.2.2.

[11]. Most importantly, it is not clear which type(s) of charge carrier is (are) responsible for SC transport in these materials. It has been suggested that studies in the UD regime could help gain more insight into the pairing mechanism in HTS materials.

To identify the responsible charge carrier in the underdoped (and, also, in the optimally doped) regime, analyses of the Little Parks (LP) measurements have to be done. Rings are highly useful structures for investigating coherent quantum phenomena in SC state, such as the Little Parks effect [12]. This effect was firstly observed in low- T_c superconductors (LTSs) [13]. In LTS systems LP oscillations are strictly $h/2e$ periodical, identifying Cooper pairs ($2e$) as the charge carriers [13] [14]. In addition to the $h/2e$ periodicity observed in LTSs, nanoscale rings patterned on HTS films are expected to show a crossover from $h/2e$ to h/e or $h/4e$ flux periodicities [15]-[20]. Due to the surface problems we encountered, we could not probe these exciting predictions in our UD films. However, we did put to a test superconductivity in nanorings in the optimal regime and, as expected, charge $2e$ carriers were found to be responsible for SC transport. Also, our measurements showed the advantage of the used patterning technique in preserving homogeneity in our rings, compared to similar work done by others [21], even though our rings are smaller in size and therefore more susceptible to damage induced by the fabrication process.

The first part of this thesis work addresses the issues related to the growth of thin YBCO films in a controllable manner with reproducible superconducting properties in the UD regime. We have succeeded in changing the T_c of the films by modifying only one parameter in the entire deposition process, that parameter being the pressure of post-annealing. The films we obtained showed not only reproducible superconducting properties, but also a high level of homogeneity, seen through rather sharp resistive normal-SC transitions. A confirmation of lower doping level in our films was found by X ray diffractometry (XRD) scans. The UD films have been deposited with the final goal of patterning and measuring devices on them, since, as stated above, the most exotic phenomena are expected for these doping levels. Unfortunately, the surface properties made our initial idea impossible to put into practice, since the submicron rings could not have been patterned on these films.

The second part of my thesis was related to fabrication of nanorings and LP measurements performed on them. Fabrication was done on optimally doped commercial YBCO

films with the idea of testing the soft nanopatterning technique previously developed in our group for nanowires' fabrication [22]. The optimization of etching conditions done in this patterning technique previously yielded 40 nm wide nanowires with highly preserved pristine SC properties as in as-grown films, reflected in the critical current density J_c approaching the theoretical depairing limit. However, the technique has never been used before for nanorings fabrication. By using it, we succeeded in patterning rings with arm's width of 90 nm but at the cost of ~ 6 K drop in T_c compared to the as-grown YBCO films.

1.2 Theoretical background

1.2.1 Conventional vs. high critical temperature superconductivity

Superconductivity, defined as the state of some materials occurring below a certain critical temperature, is described by two phenomena: resistance dropping to zero and magnetic field being expelled from the material. The last one, namely Meissner effect, is a characteristic of all superconducting materials. Whilst in Type I SC materials this is the only state allowed, in others, Type II materials, magnetic field can penetrate in form of vortices without destroying the superconducting state of the entire material. The BCS theory, explaining the microscopic mechanism behind this phenomenon, proposes a model of electron-phonon interaction which in turn results in two electrons of opposite spin and momentum overcoming the potential barrier of Coulomb repulsion and pairing up into a Cooper pair, the elemental carrier of superconductivity [8]. For materials that undergo SC transition at low temperatures (conventional or low- T_c superconductors), this theory is in agreement with experiments.

Every SC state is described by its order parameter, which contains information about the density of Cooper pairs and their unique phase. While LTSs are characterized by an isotropic s-wave order parameter, the Angle Resolved Photo Emission Spectroscopy (ARPES) reveals a different symmetry of the order parameter for HTSs. Namely, ARPES shows both gap like and

gapless like excitations in HTSs by varying the direction in the k-space. The gapless like excitations are a clear signature of the OP with nodes. This is attributed to the anisotropic crystallographic structure.

1.2.2 YBCO – structure, phase diagram and superconducting properties

YBCO represents the most studied material among HTSs. It belongs to the group of cuprates. This class of materials is characterized by the existence of CuO_2 planes, which are believed to be responsible for superconducting transport in these materials [23] [24].

The structure of $\text{YBa}_2\text{Cu}_3\text{O}_{7-\delta}$, as shown in figure 1.1, is obtained by considering three perovskite type cells stacked on top of each other. A perovskite cell consists of two types of cations (A, B) and 3 oxygen anions. In YBCO, the A cation alternates between Y and Ba (Y cation in the middle and Ba cations in the bottom and the top cell), while the B cation is Cu for all three cells. YBCO can be considered as a “defected” perovskite. Vacancy of oxygen in the Y plane and on the top and bottom planes of the cell dissolves the three-dimensional oxygen lattice leading to two sublattices with reduced dimensionality, namely the Cu_2O planes and the a-b chains.

Yttrium and Barium atoms can be considered as fully ionic (Y^{3+} and Ba^{2+}), acting as effective electron traps. Electrons found in their vicinity are localized, far from the Fermi level and, therefore, not mobile. Their role is to act as charge reservoirs for Cu_2O planes and CuO chains. Copper atoms appear as double and triple ionized cations, Cu^{2+} and Cu^{3+} , which together with oxygen O^{2-} anions, represent the mobile charge sources.

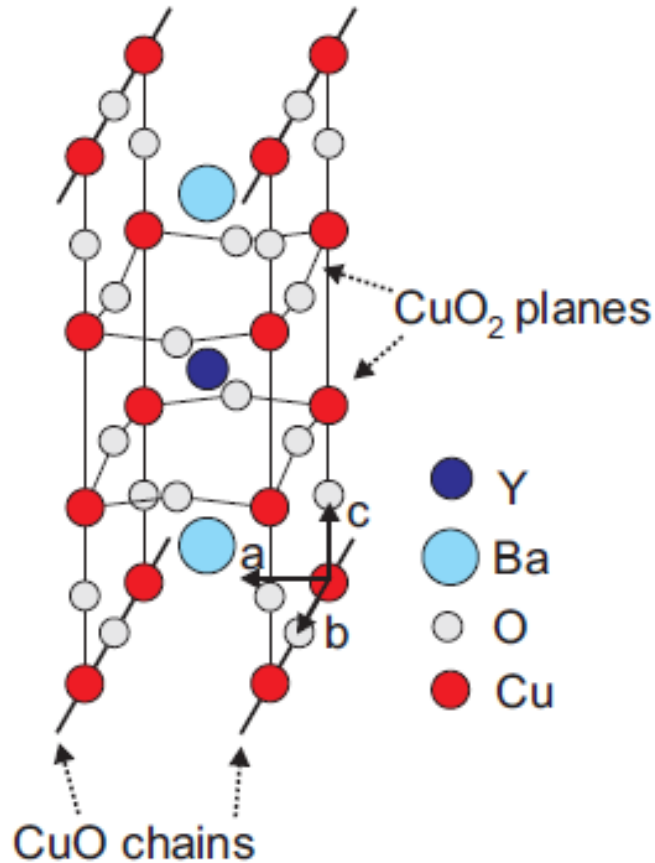


Figure 1.1: YBCO unit cell. The figure is after [25].

Structural and electronic properties of $\text{YBa}_2\text{Cu}_3\text{O}_{7-\delta}$ are dependent on the oxygen content in the unit cell (figure 1.2). The parts of the unit cell susceptible to oxygen diffusion are the CuO chains. Pumping oxygen atoms in and out of these chains modifies the YBCO properties. When CuO chains are completely deprived of oxygen ($\delta \cong 1$), YBCO is an antiferromagnetic insulator with a tetragonal structure (a and b lattice parameters equal – 0.386 nm). Oxygen doping makes YBCO conducting. This corresponds to δ decreasing from 1 to 0.

For a certain value of δ , namely around 0.6, YBCO experiences a structural change from tetragonal to orthorhombic. This means that a and b are no longer the same with b becoming slightly bigger than a , due to the injection of oxygen atoms into the CuO chains. This point marks the beginning of the region referred to as the underdoped part of the superconducting dome. At this doping level conducting properties change as well – YBCO becomes a conductor,

which below a certain temperature exhibits SC properties. Further increase in doping enhances SC properties of the material until an oxygen doping of 6.95 is reached [26]. This corresponds to $\delta \cong 0$ and the highest T_c possible (in phase diagram: top of the SC dome). YBCO containing this concentration of oxygen is referred to as optimally doped. At this doping level there are no oxygen vacancies - between every two Cu atoms in CuO chains there is one O atom. The normal state properties in this region $0 < \delta < 0.6$ (left part of the SC dome) are still not well understood. At these doping levels, above the critical temperature, in addition to gapless excitations (indication of the normal state), gap-like excitations (indication of the SC state) are found. This is one of the bottlenecks in creation of the HTS theory.

Increasing the doping level beyond the optimal point (oxygen content greater than 6.95) brings further change in conducting properties of YBCO. Namely, the normal state resembles more the Fermi metal while the SC properties get depressed (T_c reduced). This part of the SC dome is labeled as the overdoped part.

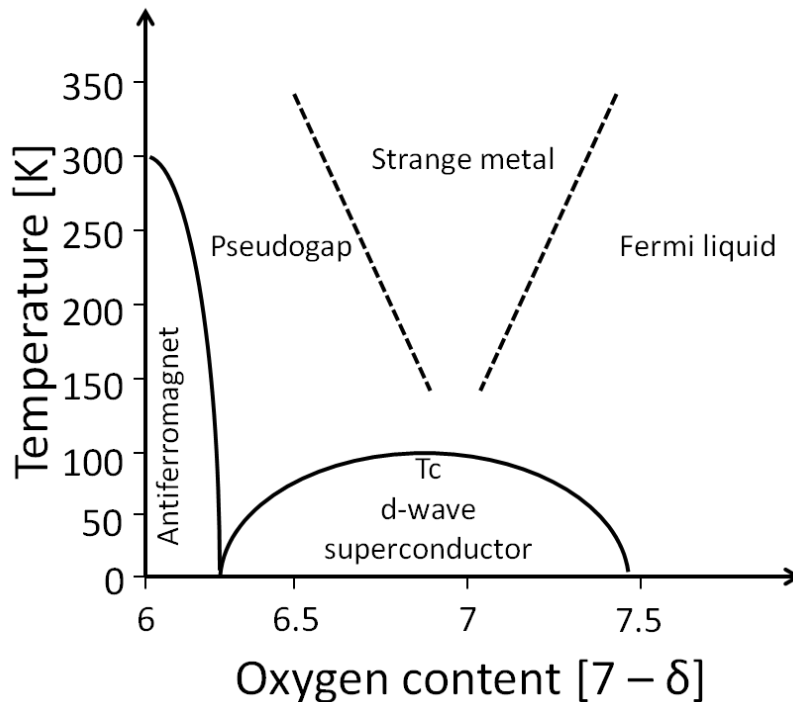


Figure 1.2: A simplified YBCO phase diagram.

Compared to conventional superconductors, YBCO has a small coherence length (ξ) and large London penetration depth (λ_L) as shown in table 1.1 (for comparison $\xi_{Nb} = 38$ nm,

$\lambda_{Nb} = 60$ nm). This makes YBCO a Type II superconductor. Below T_c there exist two distinct regions of superconductivity for these materials. Below the first critical field (B_{c1}), the superconductor is in the Meissner state. Between the first and the second critical field (B_{c2}), magnetic field enters the superconductor in a form of vortices. Vortices are normal regions whose size is determined by ξ . Magnetic field penetrates these domains with quantized flux values, corresponding to flux quanta (Φ_0). The length over which the field enters the SC material is determined by the circulating currents around the vortex core which disappear at distances larger than λ_L from the center. This state, characterized by coexistence of normal and superconducting regions, is called the mixed state. Increasing the field, the number of vortices increases until the second critical field is reached, when the distance between vortices becomes equal to the vortex core diameter and superconductivity gets completely destroyed. The lower critical field, B_{c1} , is rather low (around 0.01 T) and similar to the ones found in LTSs, while the upper one, B_{c2} , is extremely high (more than 100 T), which results in a high value for the critical current density ($\sim 10^8$ A/cm² at 4 K). High critical temperature, critical current and upper critical field make this material extremely suitable for practical applications in many superconducting devices.

Anisotropy in the YBCO structure translates into anisotropy of the characteristic SC length scales as well, namely ξ and λ_L . Anisotropy in ξ , i.e. in the size of a Cooper pair, reflects the fact that superconductivity is not equally strong in all directions, while anisotropy in λ_L , i.e. in the length over which the magnetic field penetrates the superconductor, induces anisotropy in magnetic properties of these materials.

	<i>a-b</i> (nm)	<i>c</i> (nm)
λ_L	135	1000
ξ	1.6	0.24

Table 1.1: Coherence length (ξ) and London penetration depth (λ_L) in plane (*a-b*) and along *c*-axis for the optimally doped YBCO [27] [28].

As explained above, this material has a remarkable property of switching from insulating state to a superconducting one with a broad superconducting span, by changing the doping level. The maximum T_c measured in YBCO is 92K (optimal doping) [29]. This high value cannot be

derived from the BCS theory. Another curiosity arises from the small value of the coherence length in this material [27]. Namely, coherence length not being large enough to cause the overlap of the wavefunctions belonging to electrons from adjacent CuO_2 planes, cannot be the cause for the phase coherence between the Cooper pairs in this material. There has to be another mechanism, different from the BCS one, responsible for this. Some suggest existence of an imaginary component of the order parameter in c-axis direction causing wavefunctions' overlapping [30].

1.2.3 Little Parks effect

Measurements on resistance vs. magnetic field, $R(B)$, in the vicinity of T_c (Little Parks) provide information on the value of the charge responsible for the electric transport. In particular, the period of $R(B)$ oscillations unambiguously identifies the charge carriers, which is of outmost importance for better understanding of the mechanism behind superconductivity in high- T_c materials. In addition to the $h/2e$ periodicity observed in LTSs, submicron rings patterned on HTS films are expected to show different field dependent features, namely h/e and $h/4e$ periodicities [15]-[20].

For a multiply connected (MC) superconductor (superconductor enclosing a region of a normal material or simply a hole), London introduced the concept of a fluxoid:

$$\Phi' = \Phi + \mu_0 \oint \lambda^2 \mathbf{J}_s \cdot d\mathbf{S} \quad (1)$$

with λ as the penetration depth, \mathbf{J}_s the super-current density vector, $d\mathbf{S}$ the surface vector and Φ being the ordinary magnetic flux enclosed by the loop:

$$\Phi = \oint \mathbf{B} \cdot d\mathbf{S} \quad (2)$$

(\mathbf{B} – the magnetic inductance vector).

Combining (1) and (2) with GL expressions for penetration depth and current density of a thin film:

$$\lambda^2 = \frac{m^*}{\mu_0 |\psi|^2 e^{*2}}$$

$$\mathbf{J}_s = e^* |\psi|^2 \mathbf{v}_s$$

gives:

$$\Phi' = \frac{1}{e^*} \oint (m^* \mathbf{v}_s + e^* \mathbf{B}) \cdot d\mathbf{S} = \frac{1}{e^*} \oint \mathbf{p} \cdot d\mathbf{S} \quad (3)$$

($m^* = 2m_e$ - the mass of a Cooper pair, $e^* = 2e$ - the charge of a Cooper pair, $|\psi|^2$ - the Cooper pairs' density, \mathbf{v}_s - the Cooper pairs' velocity and \mathbf{p} - the Cooper pairs' momentum in a magnetic field).

Applying Bohr-Sommerfeld motion quantization condition to relation (3):

$$\oint \mathbf{p} \cdot d\mathbf{S} = nh$$

leads to the final fluxoid expression:

$$\Phi' = n \frac{h}{e^*} = n\Phi_0 \quad (4)$$

(h - Planck's constant, n - integer)². This expression reveals the discrete nature of the fluxoid penetrating the MC superconductor. It can only exist as an integer multiple of flux quanta:

$$\Phi_0 = \frac{h}{e^*} = 2.07 \cdot 10^{-15} \text{ Wb}$$

² The expression is not a consequence of the semi-classical Bohr-Sommerfeld formalism and London equations only. It follows in the same form from the GL theory alone. The condition of the complex superconducting OP being single valued puts a constraint on the phase change around the loop which has to be a multiple of 2π : $\oint \nabla\varphi \cdot d\mathbf{S} = 2\pi n$, which results in the same condition for the fluxoid quantization.

If a magnetic field H is applied to a thin-wall cylinder with radius r , the magnetic flux inside the cylinder will be given as³:

$$\Phi = Hr^2\pi \quad (5)$$

Putting (4) and (5) into (1), the superfluid velocity is obtained as follows:

$$v_s = \frac{\hbar}{m^*r} \left(n - \frac{\Phi}{\Phi_0} \right) \quad (6)$$

For a given field H , the energy of super-currents in the cylinder will have a minimum for those values of n that allow for the minimum in the superfluid velocity v_s and that choice of n will allow the system to remain superconducting at the highest possible temperature. In this way, v_s will be a periodic function of Φ/Φ_0 (figure 1.3).

The free energy density of a thin film is given by⁴:

$$f = f_n + \alpha|\psi|^2 + \frac{\beta}{2}|\psi|^4 + |\psi|^2 \frac{1}{2} m^* v_s^2$$

where f_n is the free energy of the normal state, α the slope of the $f(|\psi|^2)$ curve in the vicinity of T_c ⁵ and β the curvature of the same curve at T_c .

Minimizing this expression for the free energy of a thin film for a given v_s , the optimum value for the superfluid density at any given position inside a superconductor is derived:

$$|\Psi|^2 = \Psi_\infty^2 \left[1 - \left(\frac{\xi m^* v_s}{\hbar} \right)^2 \right]$$

where Ψ_∞ is the SC order parameter deep inside a superconductor in the absence of the external field and transport current, and ξ is the coherence length. At the normal-SC transition, one might argue that $|\Psi|^2 = 0$, from which a constraint on ξ can be obtained:

³ No distinction should be made here between the applied field and the field inside a cylinder, since we are investigating the shift in $T_c(H)$, where $|\Psi|^2 \rightarrow 0$, so $J_s \rightarrow 0$ and the fields are the same.

⁴ Here, the field term $h^2/8\pi$ is neglected, since its value is smaller than the kinetic energy of the current by a factor of the order of the ratio of the cross-sectional area of the conductor to λ^2 and this ratio is large for thin conductors.

⁵ $\frac{df}{d(|\psi|^2)} = 0$ at T_c .

$$\frac{1}{\xi^2} = \left(\frac{m^* v_s}{\hbar} \right)^2 \quad (7)$$

From (6) and (7):

$$\frac{1}{\xi^2} = \frac{1}{r^2} \left(n - \frac{\Phi}{\Phi_0} \right)^2$$

Equating this expression with the GL coherence length near T_c for the clean limit (the mean free path larger than the coherence length⁶):

$$\frac{1}{\xi^2} = \frac{0.74 \xi_0}{\left(1 - \frac{T}{T_c} \right)^{\frac{1}{2}}}$$

one finds the expression for variations in T_c at the transition:

$$\frac{\Delta T_c(H)}{T_c} = 0.55 \frac{\xi_0^2}{r^2} \left(n - \frac{\Phi}{\Phi_0} \right)^2$$

where ξ_0 is the zero temperature coherence length. From this, the maximum depression in T_c is expected when $n - \Phi/\Phi_0 = 1/2$ and the relative variation $\Delta T_c(H)/T_c$ reaches $0.14 \xi_0^2/r^2$. It should also be noted here that the radius of the cylinder should not be very large to allow for the oscillations to be detected. Given that the rings on optimally doped YBCO films show resistive transition at ~ 80 K, and taking $\xi_0 = 1.5$ nm, cylinders with radius not larger than ~ 160 nm are required to induce T_c oscillations larger than 1 mK.

⁶ We did not perform measurements for determining the mean free path in our SC films. However, the typical values are in the range of hundreds of nm's.

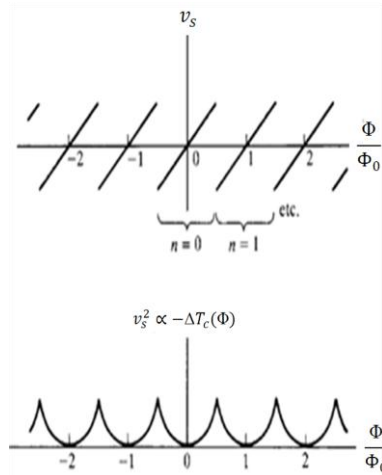


Figure 1.3: Variation of v_s (up) and v_s^2 (bottom) as a function of the magnetic field through a hollow cylinder in the LP experiment. The depression in T_c is proportional to v_s^2 (scallop shaped curve at the bottom). This figure is after [12].

In order to experimentally verify this theory, one utilizes the finite width of the resistive transition. Upon applying magnetic field near transition point the resistance oscillations are measured. Their amplitude (ΔR) can be converted to ΔT_c via the following expression:

$$\Delta T_c = \Delta R \frac{dT}{dR} \quad (8)$$

This relation is not entirely quantitatively correct, since the slope of the transition, dT/dR , has been observed to depend on the field H , causing the inferred $\Delta T_c(H)$ to depend on the resistance level choice within the transition. Still, this serves as a satisfactory method for ΔT_c extraction from LP experiments [12].

From figure 1.3, it is clear that the period of LP oscillations is determined by Φ_0 . Measurements performed so far, both on LTS and HTS structures, show this value to be the same as the one Little and Parks originally obtained: $h/2e = 2.07 \cdot 10^{-15} \text{Wb}$. This value for the flux quanta identifies Cooper pairs as the charge carriers. To argue in favor of different charge carriers responsible for transport in HTS structures, different values for flux quanta ought to be observed, since their charge enters in the denominator of the expression determining the flux quanta.

Chapter 2

Deposition and characterization of YBCO films

2.1 The substrate choice

The second part of this thesis, being the fabrication of rings scaled down to tens of nm's on YBCO films, underlines the necessity of growing homogenous films with surface roughness in the range of few nm's.

When depositing films, the substrate-film interface influences to a certain extent the morphology of the film grown. Several substrate-related factors need to be considered: lattice mismatch, thermal expansion coefficient mismatch (depositions done at high temperatures – typically several hundred °C), structural phase transitions of the substrate (twinning). The mismatch in the lattice parameter and possibly in the thermal expansion coefficient between the substrate and the material deposited represents the main source of strain and stress in films. Furthermore, if the in-plane lattice parameters (a and b) of the substrate are equal (forming a square-like pattern on the surface), twinning of YBCO films occurs when growing in c direction. Namely, the small difference of 1% between the a and b parameters of the YBCO unit cell results in an unpredictable lateral direction of growth, i.e. while stacking laterally, YBCO unit cells could experience a rotation of 90° in the plane perpendicular to the c -axis. This is reflected through the intrinsic twin domains⁷ of the YBCO. However, what proved to be a bigger challenge in growing YBCO films with good surface properties is the twinning of the substrate. This type of twinning is a different phenomenon compared to the YBCO twinning discussed

⁷ Here, a domain is defined as a c -axis grown stack of YBCO cells with a single lateral growth direction – a or b . Twin domains differ only in the lateral direction of stacking.

above and represents a temperature induced structural transition of the substrate lattice.⁸ Unlike the YBCO twinning domains, the substrate induced ones are easily visible as stripes on the YBCO films' surface. Twin boundaries in the substrate surface, when translated into the YBCO film, cause suppression of the superconducting order parameter and the critical current density [31], as well as the vortex pinning [32] and the dc flow of Abrikosov vortices under the action of the Lorentz force (the vortices move preferentially along the grain boundaries, including the twin ones) [31] [33].⁹

All of the work presented in this chapter is dedicated to YBCO deposited on Lanthanum Aluminum Oxide – LaAlO₃ (LAO) with (100) crystal orientation. LAO belongs to the group of substrates with an intrinsic problem of twinning [34] [35]. Decreasing the temperature, at 534 °C the LAO crystal lattice undergoes a structural change from a cubic type (with a lattice parameter $a = 3.82 \text{ \AA}$ at deposition temperatures around 800 °C) to the rhombohedral one (with a rhombohedral angle 90.096° and a lattice parameter $a = 3.79 \text{ \AA}$).¹⁰ The other two substrates used in this work for YBCO deposition, LSAT¹¹ and MgO, do not exhibit twinning phenomena. However, due to the time limitations within which this project had to be performed, no significant results have been obtained on LSAT and MgO.

2.2 Doping dependent YBCO films

Electronic properties of YBCO are determined by the oxygen content in the unit cell, as described in section 1.2.2. Finding the deposition conditions for the optimal growth of YBCO (highest T_c) while simultaneously optimizing the surface of the films, was the first step towards controllable underdoped films deposition. The next step was finding the deposition parameters that influence the doping level to the extent of enabling going from the top of the superconducting dome to the extremely UD regime. The deposition technique explored for

⁸ It should be noted here that the temperature induced structural transitions do not represent a characteristic of all crystals.

⁹ All these electronic and magnetic features are caused by the YBCO film twinning as well.

¹⁰ YBCO undergoes a structural transition at $\sim 400 \text{ °C}$ from a high temperature oxygen-deprived tetragonal phase (with $a = 3.86 \text{ \AA}$ and $c = 11.79 \text{ \AA}$) to an orthorhombic one (with $a = 3.82 \text{ \AA}$, $b = 3.89 \text{ \AA}$ and $c = 11.68 \text{ \AA}$) [41] [42].

¹¹ Lanthanum Strontium Aluminum Tantalum Oxide

growing SC films was the Pulsed Laser Deposition (PLD). The crystal structure of the films was subsequently characterized by the X-ray diffractometer and resistive transition detected using Physical Properties Measurement System (PPMS).

2.2.1 Pulsed Laser Deposition

Physical principles behind the PLD are described as follows. A highly energetic laser beam in the UVA range hits the target (the desired material for deposition) in pulses with duration of the order of nanoseconds. The target, being locally heated in this way, gets ablated, given that the laser energy is sufficiently high. Each pulse can be divided into two parts. In the beginning of the pulse, a vapor is formed in front of the target. During the second part of the pulse, the pressure and the temperature increase due to energy absorption, which results in partial ionization followed by the vapor expansion and formation of the plume. The plume, consisted of atoms, molecules, ions, electrons and atomic clusters, condenses on the heated substrate placed against the target (figure 2.1).

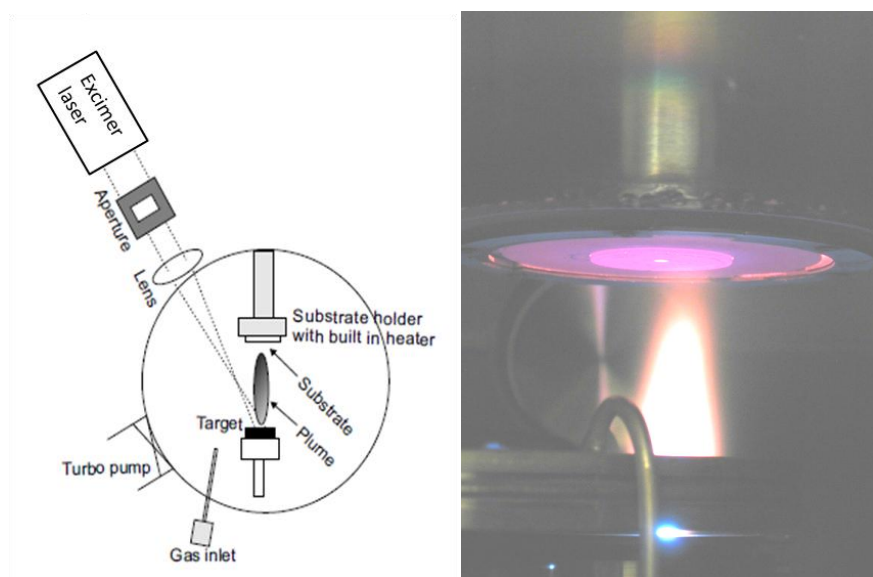


Figure 2.1: A sketch of the PLD system (taken from [36]) used for the YBCO deposition (left) and a picture of the plume inside the chamber during the deposition (right).

Many deposition parameters influence the final characteristics of the film growth: the fluence of the laser beam (ratio between the energy of the beam and the surface of the focal point on the target), the pulse rate, the distance between the target and the substrate, the background gas pressure, the temperature of the substrate. Finding the right set of values for all these parameters in order to obtain a film with desired doping and surface properties is a challenging task. Another difficulty reflects in the fact that the optimal growth on different substrates requires different deposition conditions.

The key property of the plume susceptible to all of these parameters is the kinetic energy of the atoms and ions reaching the substrate. The growth of homogeneous, relaxed, defect-free films is actually confined to a narrow energy range. If the kinetic energy is very high, re-sputtering from the film can occur, while, on the other hand, if it is too low, the atoms/ions do not have enough mobility to rearrange themselves on the surface. While the aforementioned parameters affect the kinetics of the particles between the target and the substrate, the substrate temperature affects their surface kinetics. Again, a range of temperatures is allowed to grow high quality films. If the temperature is too high, interdiffusion between the substrate and the film can occur; if the temperature is too low, the atoms/ions will not be mobile enough to find the best site to occupy. As will be shown later, the deposition temperature has a large influence on the smoothness of the films' surface.

For the purposes of this thesis, 50 nm YBCO films were deposited which was followed by an ex-situ 50 nm gold (Au) film evaporation soon afterwards to protect the YBCO films from oxygen diffusion.

The highest T_c obtained in YBCO films was reported on LAO substrates with 001 crystal orientation (~ 92 K). In our films, the highest onset temperature for the normal – superconducting transition found was 91.3 K with a transition width of 1.6 K (table 2.1 – sample nr. 1). This film was deposited under the pressure of 0.6 mbar at 865 °C. Slow cooling rate followed, with one hour of post-annealing at 550 °C. After the deposition, the pressure in the chamber was set to 650 torr and the sample was held at that pressure until the temperature fell below 50 °C. This sample will be referred to as the optimally doped one from now on.

2.2.2 Characterization of YBCO films

2.2.2.1 Electronic properties

The oxygen content of the YBCO unit cell proved to be mostly dependent on the post-annealing procedure. Data on the deposition conditions used and the corresponding resistive transitions of the films are shown in Table 2.1. The $R(T)$ measurements performed on some of these samples are presented in Figure 2.2.

Sample number	T_d [°C]	p_d [mbar]	p_{pa} [torr]	$CDR I$ (865 – 550) °C [°C/min]	t_{pa} [min]	$CDR II$ (550 – 50) °C [°C/min]	T_{onset} [K]
1	865	0.6	$6.5 \cdot 10^2$	10	60	15	91.3
2	865	0.6	$6.5 \cdot 10^1$	10	60	15	91.1
3	865	0.6	$6.5 \cdot 10^0$	10	60	15	91.1
4	865	0.6	$6.5 \cdot 10^1$	30	1	40	90.8
5	865	0.6	$6.5 \cdot 10^0$	30	1	40	91.2
6	865	0.6	$4.5 \cdot 10^{-1}$	30	1	40	90.4
7	865	0.6	$4.5 \cdot 10^{-2}$	30	1	40	87.6
8	865	0.6	$2 \cdot 10^{-2}$	30	1	40	83.7
9	865	0.6	$1.5 \cdot 10^{-2}$	30	1	40	82.3
10	865	0.6	$1.2 \cdot 10^{-2}$	30	1	40	72
11	865	0.6	$1 \cdot 10^{-2}$	30	1	40	63.6
12	865	0.6	$7.5 \cdot 10^{-3}$	30	1	40	62
13	865	0.6	$4.5 \cdot 10^{-3}$	30	1	40	58.8

Table 2.1: Summary of the c-axis oriented YBCO 50 nm films deposited on LAO (001): deposition conditions - temperature (T_d), pressure (p_d); post-annealing parameters – pressure (p_{pa}), Cool Down Rates ($CDRs$) I and II, post-annealing time at 550 °C (t_{pa}); transition parameters – transition onset temperature (T_{onset}).

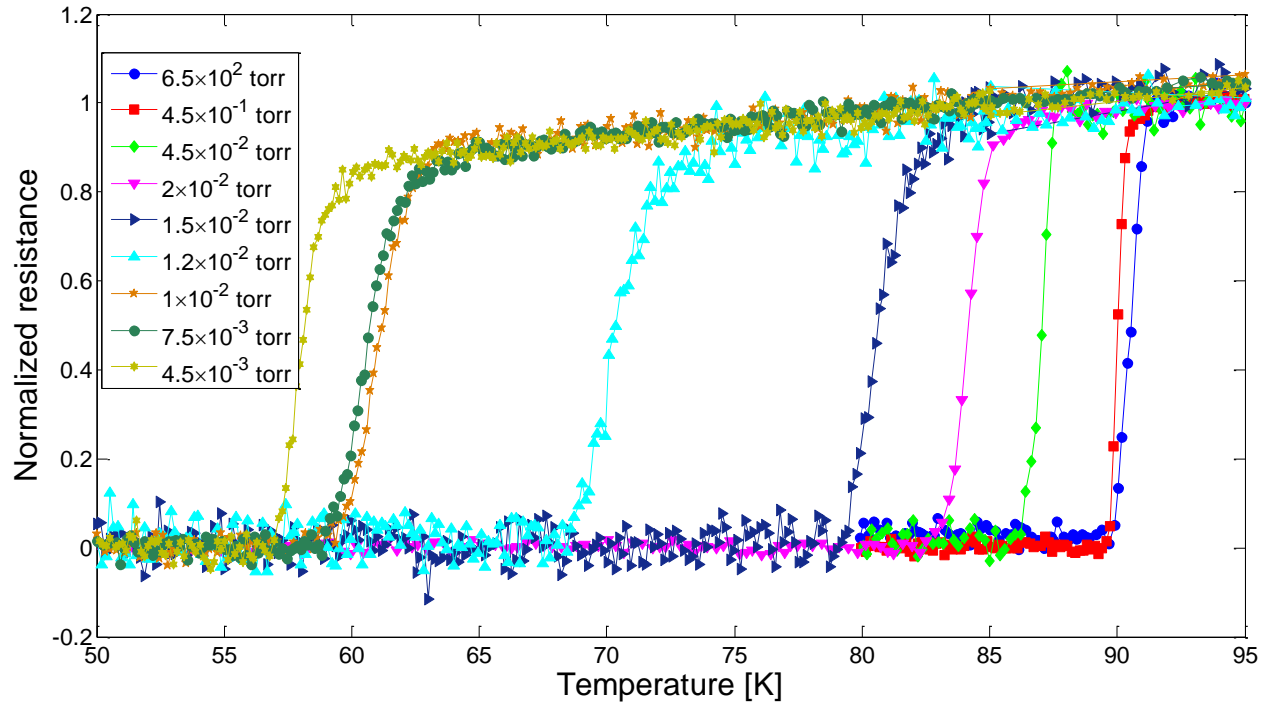


Figure 2.2: Resistive transition measurements on nine 50 nm c-axis oriented YBCO films deposited on LAO (001) with different post-annealing pressures, ranging from $6.5 \cdot 10^2$ torr (optimally doped YBCO) to $4.4 \cdot 10^{-3}$ torr (YBCO film with the lowest doping). The resistances are normalized with respect to resistance values at 95 K (normal resistance).

Decreasing the post-annealing pressure by factors of 10 and 100 (compared to the optimal film) resulted in almost the same onset temperature (samples nr. 2 and 3). No change was observed for these pressures by increasing the post-annealing cooling rate (samples nr. 4 and 5). By decreasing the post-annealing pressure by another factor of 10 (making it equal to the deposition pressure) and keeping the faster cooling rate, a very sharp transition (< 1 K) was observed with a drop in T_c of almost 1 K (sample nr. 6). All the subsequent samples (as well as the three previous ones) were characterized by a post-annealing procedure with a fast cool down with only 1 min of post-annealing at 550 °C. Decreasing the post-annealing pressure by another factor of 10 resulted in the first significant drop in T_c (~ 4 K) compared to the optimal film

(sample nr. 7). The most pronounced changes of T_c were observed to happen in a very narrow range of pressures: $4.5 \cdot 10^{-2}$ - $4.5 \cdot 10^{-3}$ torr (figure 2.3).

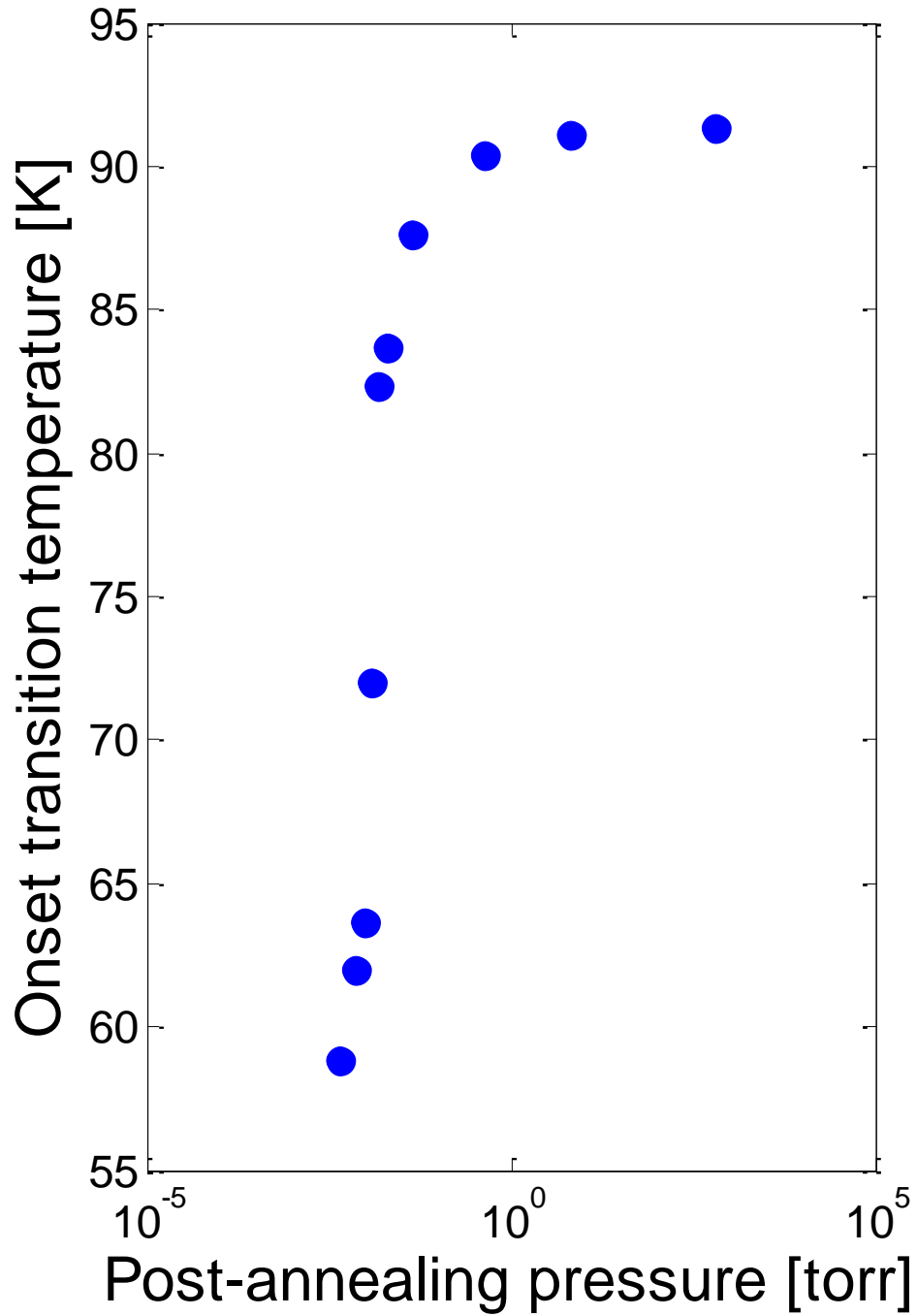


Figure 2.3: Onset transition temperature of YBCO films deposited with different post-annealing pressures (presented in a log scale).

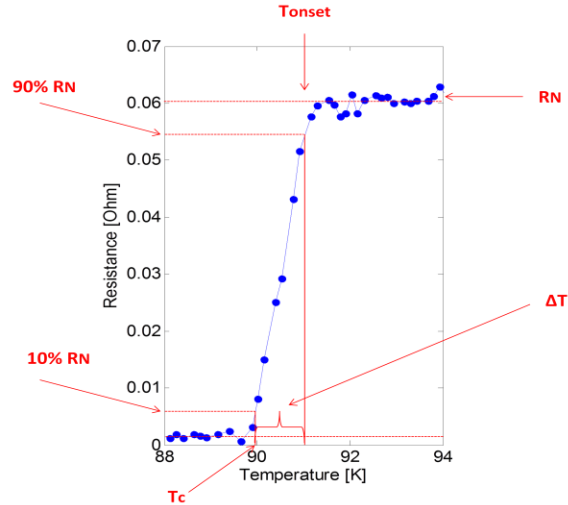


Figure 2.4: Graph illustrating the definition of the transition width (ΔT) given as the difference between the onset transition temperature (T_{onset}) and the critical temperature (T_c). T_{onset} and T_c are defined as temperatures at which the resistance drops to 10% and 90% of the normal state resistance (R_N), respectively.

T_{onset} [K]	ΔT [K]
91	1.6
91	1.2
90	0.9
87	1.4
83	2.7
82	2.6
72	3.4
63	3.6
62	3.3
58	1.8

Table 2.2: Transition widths (ΔT) corresponding to the onset transition temperatures (T_{onset}) of YBCO films presented in Figure 2.2.

Low values of ΔT (table 2.2) indicate sharp resistive transitions, characteristic of highly homogeneous films. A trend in ΔT increase is observed when going deeper into the UD regime. Small doping variations in the film could account for this, given that the slope of the SC dome increases when moving from the (flat) optimally doped part to the UD one (figure 1.2).

An attempt to observe SC transition below $4.5 \cdot 10^{-3}$ torr failed. Namely, we deposited two films under the same conditions as for the other UD films, but with post-annealing at $1.5 \cdot 10^{-3}$ torr and $2 \cdot 10^{-6}$ torr. The films showed metallic behavior down to 4 K.

2.2.2.2 Crystallographic properties

When pumping out oxygen atoms from the CuO chains of the YBCO unit cell, the cell expands in the c -axis direction. To study the structural deformation of the YBCO unit cell in our UD films, XRD $2\theta - \omega$ scans were done on the optimally doped film and several UD ones (figures 2.5 and 2.6).

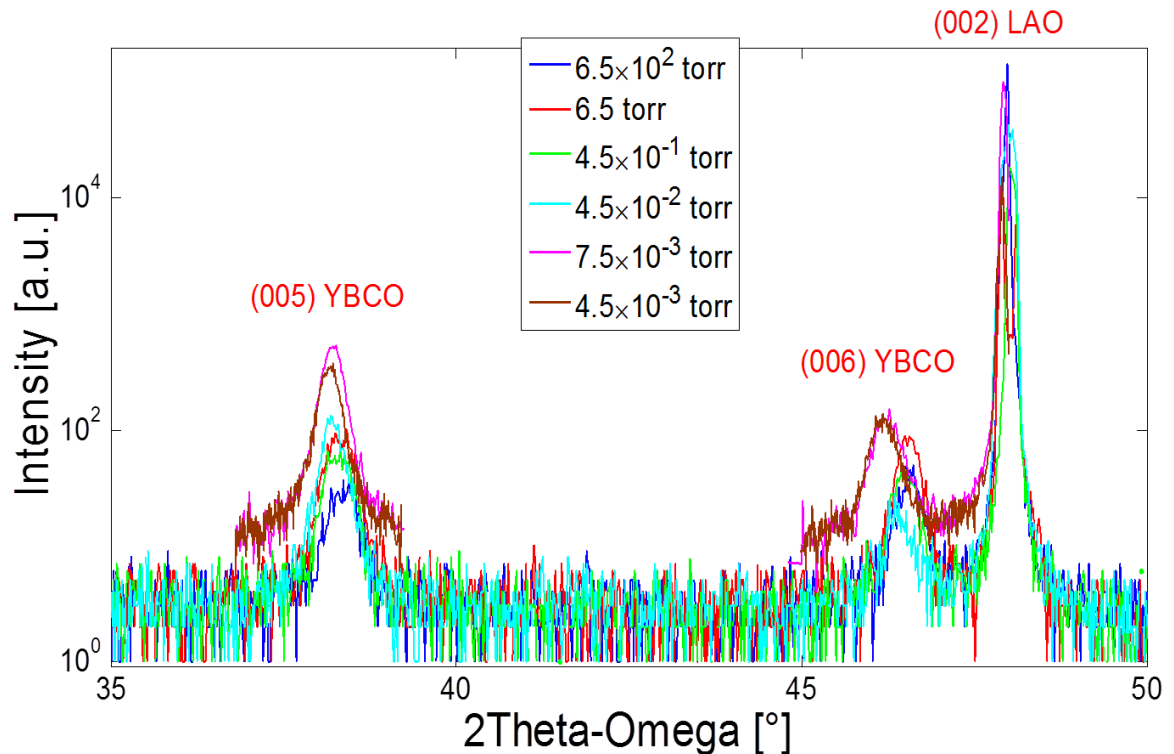


Figure 2.5: $2\theta - \omega$ scans performed on six YBCO films with different post-annealing pressures. Three peaks are observed in the $(35-50)^\circ$ range of the 2θ angle: the (005) YBCO and (006) YBCO reflections and the (002) LAO. Shift to the left is observed for every peak as the pressure decreases.

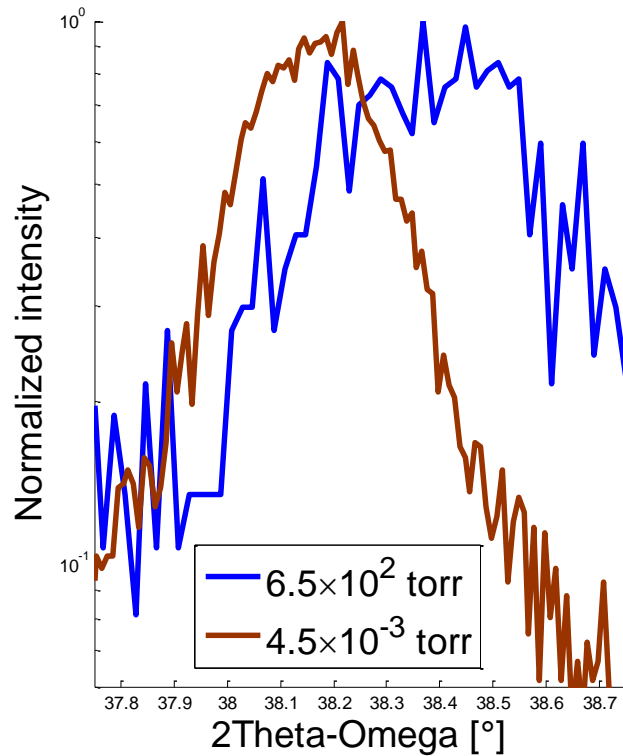


Figure 2.6: (005) YBCO peak from $2\theta - \omega$ scans performed on the optimally doped (blue) YBCO film and the most underdoped (brown) YBCO film. A shift to the left, corresponding to the increase of the YBCO unit cell height, is observed in the UD film compared to the optimal one.

From Bragg's law, it follows that the distance between the crystallographic planes is inversely proportional to the angle at which a peak of certain order is observed¹². So, the scans in figures 2.5 and 2.6 show an expansion of the YBCO unit cell in a direction perpendicular to the CuO_2 planes with the decrease in the post-annealing pressure. This serves as a definite proof that by changing only the post-annealing pressure we obtained YBCO films with different oxygen concentration. XRD data on underdoped YBCO films are summarized in table 2.3 and figure 2.7.

¹² For further information on XRD system and measurements, the reader is referred to Appendix A (XRD).

Sample number	Post-annealing pressure [torr]	YBCO unit cell height [Å]
1	$6.5 \cdot 10^2$	11.69
3	6.5	11.7
6	$4.5 \cdot 10^{-1}$	11.72
7	$4.5 \cdot 10^{-2}$	11.74
12	$7.5 \cdot 10^{-3}$	11.764
13	$4.5 \cdot 10^{-3}$	11.783

Table 2.3: YBCO unit cell height obtained from the $2\theta - \omega$ scans of the (005) YBCO peak on films with different post-annealing pressures.

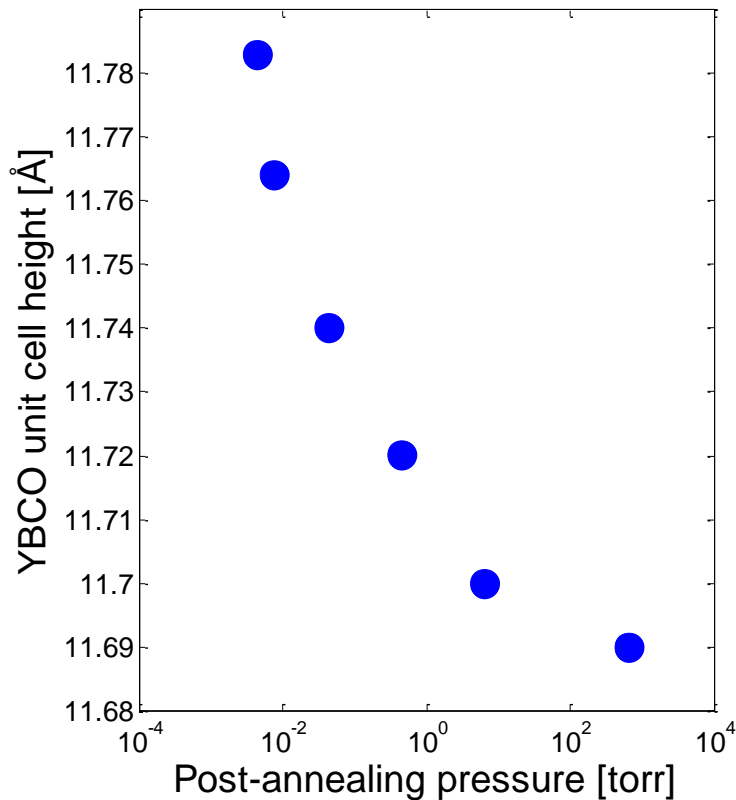


Figure 2.7: YBCO unit cell height as a function of the post-annealing pressure (samples from the Table 3.2). The data is presented in a log scale.

2.2.2.3 Surface properties

When depositing superconducting films, one needs to reach compromise conditions for obtaining films with the desired SC properties and good enough surface properties for device patterning. Our YBCO films deposited by PLD show that these two requirements are somewhat conflicting, i.e. improving the surface of the film leads to lower T_c and wider transition, compared to the case when no surface optimization was done.

Scanning Electron Microscope (SEM) pictures were taken on several films. SEM images on the optimally doped film and one of the underdoped ones are presented in figure 2.8. These scans show particle-like features on our surfaces, as well as oriented domains. The origin of the particle-like features is still under investigation. On the other hand, the oriented domains are a signature of an a-axis growth of YBCO. Their elongated appearance comes as a consequence of growth velocities having different values in different directions (a , b , c). The size of the surface features varies from tens of nm's (particles) to several μm 's (particles and a-axis domains). An increase in particles' density was noticed with a decrease in the post-annealing pressure. As mentioned in section 2.2.2.1, a loss of superconducting behavior in UD films is observed below $4.5 \cdot 10^{-3}$ torr. We attribute this to very bad surface conditions in the UD regime which could easily result in formation of regions of non-SC material enclosing entire loops that could account for metallic behavior down to very low temperatures.

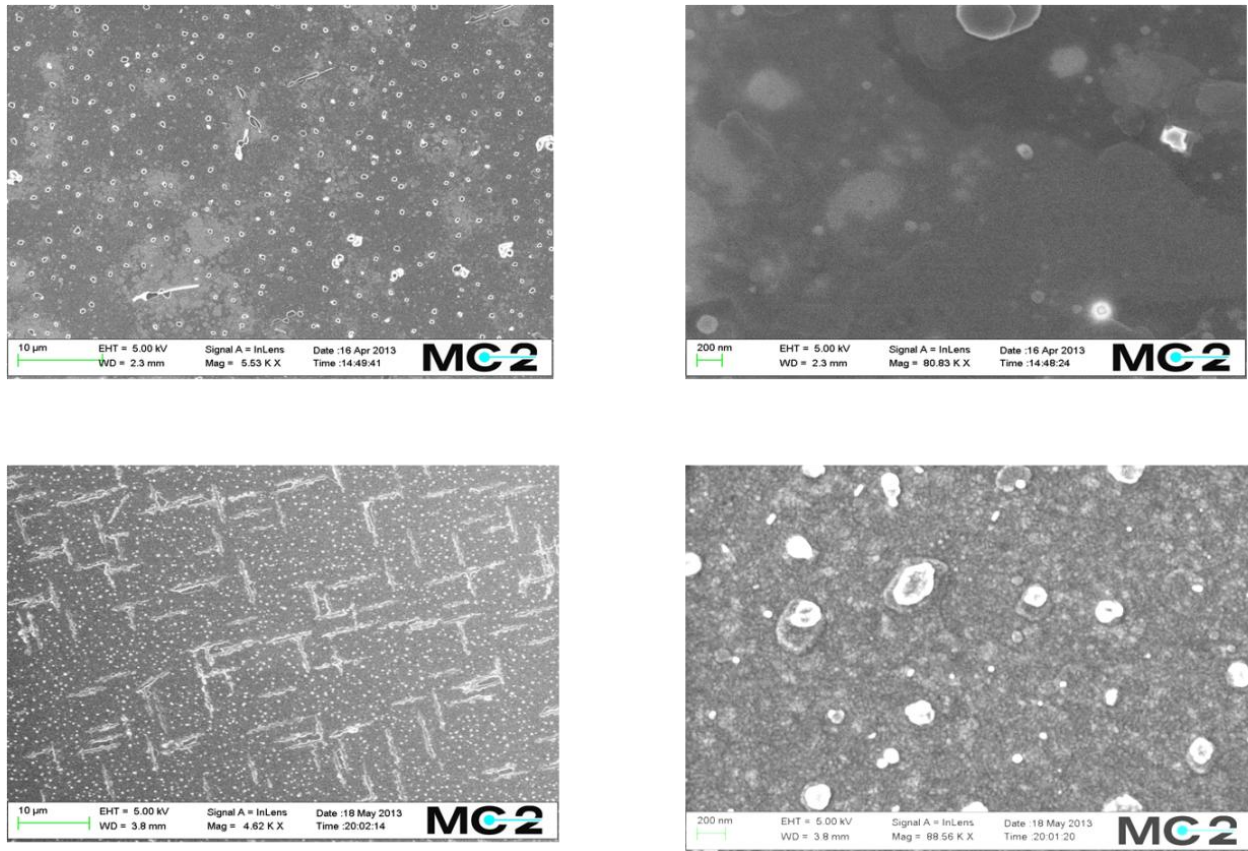


Figure 2.8: SEM pictures of the optimally doped (up) YBCO film ($6.5 \cdot 10^2$ torr) and underdoped (down) YBCO film ($4.5 \cdot 10^3$ torr) before surface optimization. The scans on two comparable length scales are presented (left – larger, right – smaller).

Regardless of the lack of knowledge on the origin of these surface shapes, some improvements have been made in depositing films with smoother surfaces. Different approaches have been used - changing the energy of the laser, its pulse rate, the substrate-target distance. However, the parameter that proved to influence the surface properties the most was the temperature during the deposition (T_d). After several chamber passivations, by decreasing T_d from 865 °C to 780 °C, we obtained better surface properties for YBCO grown on LAO (figure 2.9). From this figure, it is clear that more work on optimizing the deposition conditions for better surfaces is needed, especially for UD films.

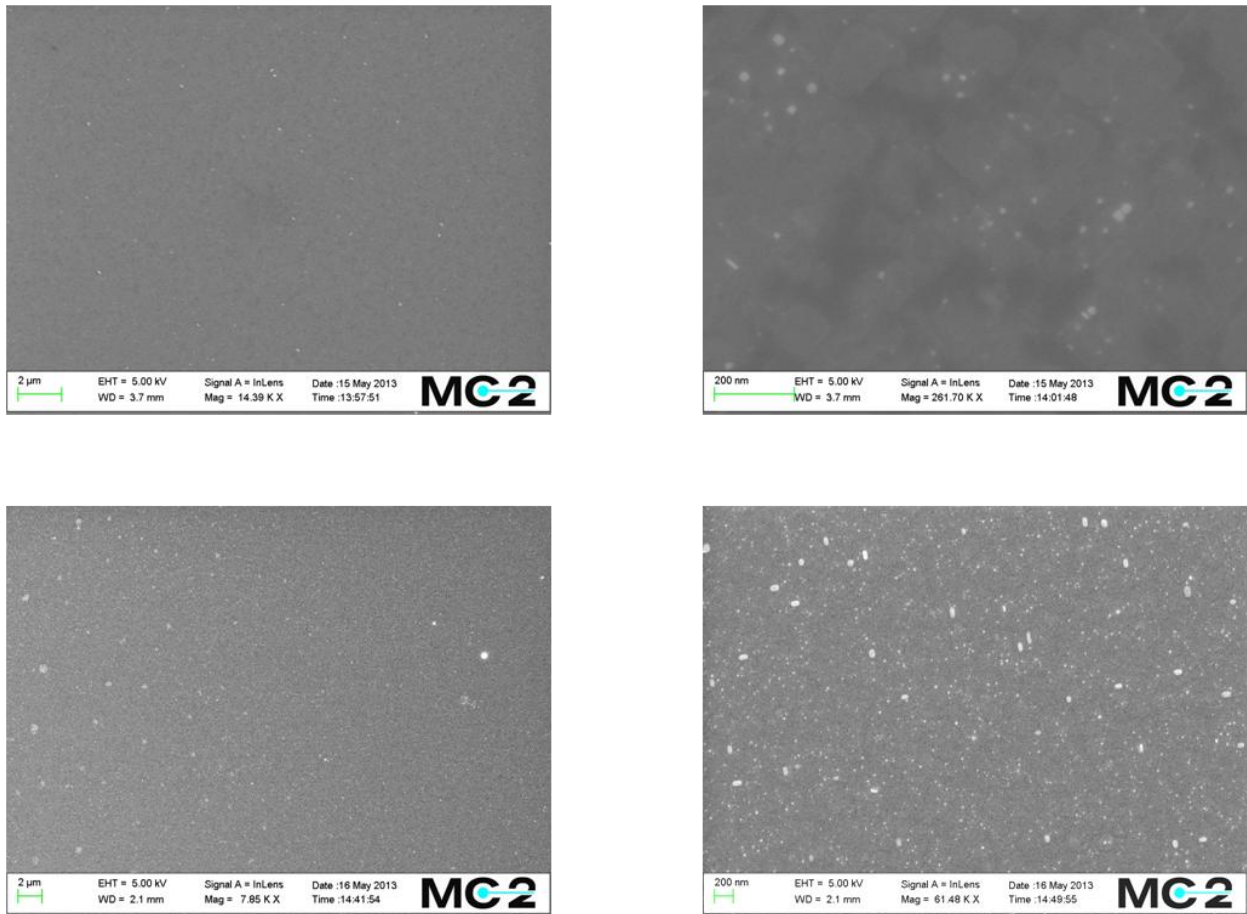


Figure 2.9: SEM pictures of the optimally doped (up) YBCO film ($6.5 \cdot 10^2$ torr) and underdoped (down) YBCO film ($1 \cdot 10^{-2}$ torr) after first attempt of surface optimization (several passivations and a deposition temperature decrease). The scans on two comparable length scales are presented (left – larger, right – smaller).

Chapter 3

Fabrication of optimally doped YBCO nanorings

Nanofabrication process used to pattern YBCO films is depicted in figure 3.1.

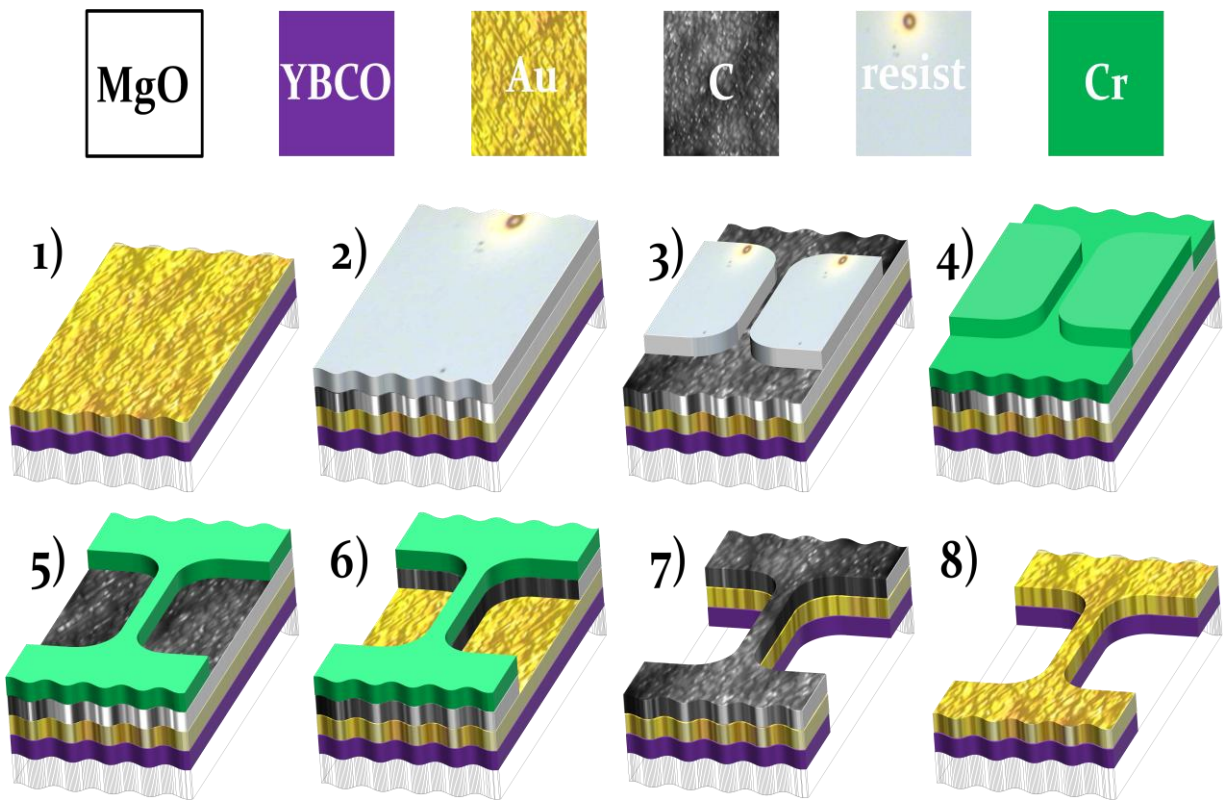


Figure 3.1: Nanofabrication scheme used for YBCO nanorings, displaying the most important steps: 1) YBCO deposition and gold evaporation; 2) carbon (C) evaporation and double-layer resist spin coating; 3) resist development after e-beam lithography; 4) chromium (Cr) evaporation; 5) Cr lift off; 6) oxygen (O) plasma etching of the uncovered C; 7) Ar⁺ ion beam etching; 8) O plasma removal of the residual C.

The method we used for deposition of YBCO films resulted in obtaining films with reproducible SC properties. However, the surface properties were substantially worse, making patterning of nanodevices impossible. Regardless, we wanted to test the fabrication procedure optimized previously in our group for the fabrication of nanowires to realize nanorings. We resorted to using commercial (001) YBCO films produced by THEVA. This company produces only YBCO films close to the optimally doped regime.

The THEVA YBCO films used had a 30 nm thickness, were c-axis oriented, grown on (100) MgO and covered with 30 nm of gold (Au). The films had a T_c of 87 K and a sharp transition with a width of 1 K.

Detailed description of all the steps with the relevant used parameters is given below:

- a) Additional 20 nm of Au was evaporated on top of the YBCO/Au bilayer after isopropyl alcohol (IPA) and nitrogen (N) cleaning. The layer of Au disables oxygen diffusion out of YBCO and protects the film from contamination and physical damage caused by the subsequent fabrication steps.
- b) As hard mask, we used an 80 nm amorphous C layer. The deposition chamber for the evaporation of C was pumped down to $\sim 2 \cdot 10^{-7}$ mbar, followed by a C target pre-ablation (needed to clean the target) and titanium (Ti) ablation (needed to decrease the pressure after the C pre-ablation) which provided the recovery of the previous base pressure of $\sim 2 \cdot 10^{-7}$ mbar at which the C deposition was finally done. The evaporation rate was rather low (~ 1 nm/s) to ensure uniformity of the C film.
- c) Low power oxygen plasma etching (50 W) was performed for 5 s to clean the surface from undesired particles coming from the C evaporation chamber.
- d) IPA cleaning in the spin coating machine was done prior single-resist spinning. The resist ZEP 520 A 1:1 was spun and baked at 95 °C for 7 min. The thickness of the resist is directly related to the spinning speed. We achieved a thickness of ~ 100 nm with the speed of 5500 rpm.

-
- e) Nanostructures were defined by e-beam lithography (EBL) at 100 kV. The steps after e-beam exposure are crucial for getting reproducible structures at nanoscale.
 - f) The exposed part of the resist was developed in hexylacetate for ~ 20 s followed by a short rinsing of 3 s in IPA to stop developing. This creates an undercut in the developed structure that facilitates the lift-off.
 - g) Low-power oxygen plasma etching (50 W) was performed for 5 s to clean the surface from residual parts of the exposed resist.
 - h) A thin layer (12 nm) of chromium (Cr) was evaporated with a low evaporation rate (1 \AA/s).
 - i) Lift-off of Cr on the top of the remaining resist was done in a 1165 removal at 50°C for ~ 15 min followed by ~ 10 s in a low-power ultrasonic bath. Additional ~ 5 min of removal in the 1165 bath and 3 min of rinsing in IPA were done to ensure complete removal of the unexposed resist.
 - j) Low-power oxygen plasma etching (50 W) was performed for 22 min to remove the C not covered by Cr.
 - k) Argon (Ar) ion etching was used to remove the Au and YBCO layers' parts not covered by Cr. The ion etching parameters need to be well controlled, since high power argon ions (Ar^+) can change severely the film stoichiometry. Small changes in etching parameters proved to strongly affect the transport properties of nanostructures, in particular the critical current (I_c) and its dependence on T_c . So, the acceleration voltage was chosen high enough to etch the film (below that value the film is not etched but made amorphous), while the etching time is calibrated so to minimize Ar^+ ions interaction with YBCO/Au rings. For our rings, we used ~ 60 min etching with an accelerating voltage of 300 V and a current density of 0.056 mA/cm^2 , at a chamber pressure of $1.6 \cdot 10^{-4}$ mbar. During the etching, the Cr over the structures is removed, as well as part of the C. Atomic Force Microscope (AFM) pictures of our rings showed an over-etch of ~ 10 nm in the substrate.
 - l) Low power oxygen plasma etching (50 W) was performed for 18 min to remove the remaining C on top of the rings.

Having a protective Au layer during the fabrication and not removing it at the end of the process, has proven to help in preserving the pristine SC properties of YBCO in nanostructures comparable to the as-grown films [22].

Chapter 4

Transport measurements

Rings are useful tools when investigating quantum effects coming from the mesoscopic confinement of the superconducting state. In particular, Little Parks measurements on superconducting rings reveal the type of charge carrier in these materials. Previously, in high- T_c materials, LP was measured on micron sized hole arrays [37] and single rings with inner diameters and arm widths of the order of hundreds of nanometers [21]. An array of nanorings can introduce artifacts in the measurement due to the higher order harmonics, which appear when flux quanta enter not just the measured ring, but also several other cells in the array. In a single loop, on the other hand, there is no convolution of the fundamental period of the loop with the periods coming from other cells and therefore, intrinsic effects related to the magnetoresistance (Little Parks) in a single loop can be more easily distinguished. Here, we report on LP measurements on single YBCO rings with dimensions that have not been reached before (inner diameter and arm width smaller than 100 nm).

Rings with several different submicron sizes have been patterned on 30 nm thick optimally doped YBCO films. Five nanorings have been measured, selected from three different chips, with different inner diameters and arm widths. In this chapter, isothermal magnetoresistance (MR) measurements on two rings which differ to the largest extent geometrically (inner diameters of 70 nm and 260 nm and arm widths of 160 nm and 90 nm, respectively), will be presented. The resistance vs magnetic field measurements were performed at several temperatures of the resistive transition of these devices above T_c , which is defined here as the temperature below which the measured resistance becomes smaller than the noise level of the measurement set-up. No resistive transition of the larger YBCO areas, such as wiring and pads, was observed, as expected, considering the resistance was measured in a four probe

configuration¹³. Four electrodes, two voltage and two current ones, were attached closely to the rings (tens of nm's distance), so as to detect the resistive transition of the rings only.

The resistance has been measured as a function of the magnetic field at several temperatures between T_c and the onset transition temperature. We selected a (-0.2 – 0.2) T field range (low field), in which several oscillations are observed. Obtained resistance oscillations in this field range were superimposed on a parabolic background coming from the screening currents in the arms of the rings [38]. In the wider ring (figure 4.2), more clear oscillations have been observed in a narrower field range: (-0.1 – 0.1) T, so the further analysis of the data for this ring followed on this range only (due to negligible background noticed in the data for the narrower ring, presented in figure 4.3, the data from the entire field scan range was used without parabolic subtraction for that ring). The background (in the case of the wider ring) was subtracted by a parabolic fit of the form:

$$R_{fit} = aB^2 + bB + c$$

with $a, b, c \neq 0$. Using a three-parameter fit takes into account not only the curvature in the data (parameter a), but also a zero-field shift (parameter b) and average resistance (parameter c) which increases upon moving from a T_c point towards T_{onset} , i.e. upon approaching the normal state. Obtained plain oscillations were a subject of a Fast Fourier Transform (FFT) analysis. FFT spectrum of $R(B)$ oscillations reveals the period of MR oscillations:

$$\Delta B = \frac{\Phi_0}{r^2\pi} \quad (9)$$

with r being the radius of the SC loop enclosing the flux Φ_0 in the ring (cylinder). The type of the charge carrier responsible for coherent transport in the ring can be now readily inferred by comparing the value obtained for Φ_0 from (9) with the following expressions:

$$(\Phi_0)^e = \frac{h}{e}, \quad (\Phi_0)^{2e} = \frac{h}{2e}, \quad (\Phi_0)^{4e} = \frac{h}{4e} \quad (10)$$

In all our rings, measurements displayed $h/2e$ periodicity of the magnetic flux enclosed by loops with diameters equal or close to the average ones obtained by AFM. Given that the rings were

¹³ For further information on the measurement system, the reader is referred to the Appendix B (PPMS).

patterned on the optimally doped films, no other types of periodicity (e or $4e$) were expected to present themselves.

A potential uncertainty in data analysis related to inadequate geometrical design of the rings needs to be noted here. FFT spectrum is given as a function of $1/B$ and the peak position corresponding to a certain type of a charge carrier is given as a reciprocal value of the expression defined by (9). Therefore, from (9) and (10) it is clear that the FFT peak position ($1/\Delta B$) is proportional to the squared radius of the superconducting loop r^2 and to the charge value of the carrier in question (e , $2e$ or $4e$). Due to the finite width of the ring, in order to avoid an overlap of the regions in which the three different periodicities (h/e , $h/2e$ and $h/4e$) are expected to appear, the following conditions have to be fulfilled:

$$\left(\frac{1}{\Delta B}\right)_{max}^e = \left(\frac{1}{\Delta B}\right)_{out}^e \leq \left(\frac{1}{\Delta B}\right)_{in}^{2e} = \left(\frac{1}{\Delta B}\right)_{min}^{2e}$$

$$\left(\frac{1}{\Delta B}\right)_{max}^{2e} = \left(\frac{1}{\Delta B}\right)_{out}^{2e} \leq \left(\frac{1}{\Delta B}\right)_{in}^{4e} = \left(\frac{1}{\Delta B}\right)_{min}^{4e}$$

where subscripts *in* and *out* refer to the inner (r_{in}) and outer (r_{out}) radius of the ring (figure 4.1). Both conditions, in combination with (9) and (10), give rise to the following requirement on r_{in} and r_{out} :

$$\frac{r_{out}}{r_{in}} \leq \sqrt{2} \quad (11)$$

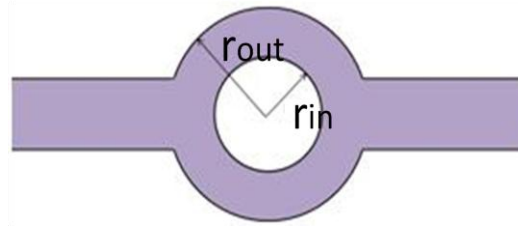


Figure 4.1: A sketch of the nanoring with current leads.

For a fixed arm width of the ring, $w = r_{out} - r_{in}$, condition (11) puts a lower bound for the inner diameter¹⁴:

$$d_{in} = 2r_{in} \geq 2(1 + \sqrt{2})w \quad (12)$$

In the ring #1 (wider ring), whose dimensions after patterning (figure 4.2a) do not comply with the relation (12), an overlap of regions in which h/e and $h/4e$ periodicities could appear with the $h/2e$ peak position takes place, so it is not possible to state unequivocally which type of charge carriers is responsible for the transport properties based on MR measurements on this ring only (figure 4.2e). In the ring #2 (narrower ring), where dimensions (figure 4.3a) are closer to fulfilling the condition (11), the overlap between the three periodicity regions does not occur in the position of the $h/2e$ peak (figure 4.3d). Based on the facts that the two rings were patterned on the optimally grown YBCO and that they differ only in dimensions, one could argue that the superconductivity observed in both rings is established by Cooper pairs and no other type of carriers.

Due to the nanofabrication limitations which do not allow for patterning of structures with feature dimensions as small as the coherence length in HTSs, detection of T_c vs magnetic field oscillations is somewhat challenging in these materials, given the amplitude of these oscillations is proportional to $(\xi_0/r)^2$. As stated in 1.2.3 section, measured resistance oscillations can be related to the T_c oscillations via relation (8). Amplitude of T_c oscillations (ΔT_c) depends on the temperature at which the MR was acquired. The largest ΔT_c values obtained in our rings, 80 mK, are 1-2 orders of magnitude larger than the values predicted by the theory for clean superconductors, $0.14\xi_0^2/r^2 \sim (1 - 2)$ mK, assuming a zero-temperature coherence length of 1.5 nm. This large discrepancy is consistent with previous measurements on HTS structures [37] and conventional systems [38] and has been attributed to the fact that in theory sharp resistive transitions are considered [38], whilst the R(T) characteristics of submicron rings on thin films typically have a broader transition.

¹⁴ It should be mentioned here that conditions (11) and (12), even though valid, are not important for our rings, considering that they have been patterned on optimally doped YBCO, in which one does not expect e nor $4e$ charge carriers. The fulfillment of the condition stated through (11) and (12) will be necessary for rings patterned on underdoped films.

Contrary to the results previously reported on HTS rings with sizes comparable to ours [21], our measurements show no additional periodic peaks in the FFT spectra of the R(B) data. Moreover, our peak is displayed with a width ~ 8 times narrower. Both of these improvements we achieved could be ascribed to the soft-patterning technique we used and the Au layer which was not removed from the YBCO structures even after the fabrication was completed. It is our belief that due to these reasons, we maintained the homogeneity of YBCO films after patterning with smaller number of regions with suppressed superconducting properties as compared to previous works [21].

As reported previously [21], to avoid a situation of rings becoming superconducting while current leads being normal, we made the current leads larger compared to the arm width of the rings, as can be seen in figures 4.2a and 4.3a. This allows for non-equilibrium effects induced by the normal leads and responsible for critical current enhancement near T_c and order parameter suppression at lower temperatures [39], to be negligible compared to the shielding currents in the loop responsible for the LP effect.

Detailed description on the measurement results for each ring is given under the corresponding figure (figures 4.2 and 4.3).

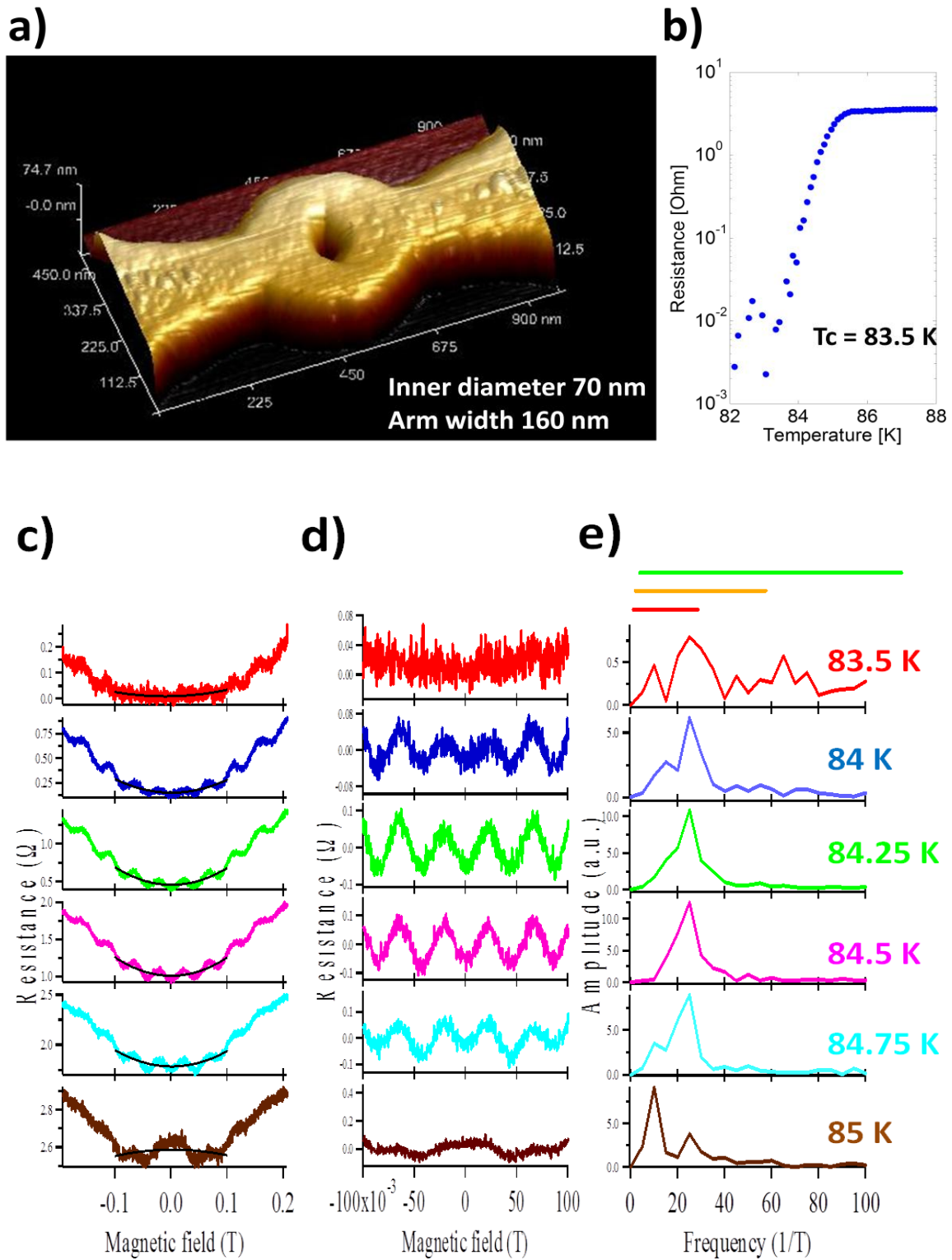


Figure 4.2: Ring on the optimally doped 30 nm 001-oriented YBCO on 100-cut MgO (film #1).

(a) AFM picture (inner diameter 70 nm; arm width 160 nm; average roughness < 1 nm). (b) The corresponding resistive transition of the ring ($T_c \sim 83.5$ K). (c) Resistance measurements at six temperatures above T_c in the (-0.2 – 0.2) T magnetic field span. Parabolic fits in the (-0.1 – 0.1) T field range are depicted by black lines. (d) Resistance oscillations in the (-0.1 – 0.1) T field range obtained after subtracting the parabolic fit ($\Delta T_{cmax} \sim 80$ mK $\gg \Delta T_{ctheory} \sim 2$ mK)¹⁵. Note that at the lowest temperature, the oscillations are not clear due to the fact that at that temperature, the resistance of the ring, being almost at T_c , is comparable or smaller than the noise level. Also, in the FFT spectrum of the MR oscillations, a low frequency component appears. It is very pronounced at the lowest temperature and even larger than the $h/2e$ peak at the highest temperature. The presence of this component is not connected to any intrinsic properties of the ring. On the contrary, its origin lies in parabolic fitting curve subtraction. Another peculiarity has been observed in the collected MR data for this ring. Namely, the peak that occurs at the highest temperature, coming from the maximum in resistance at zero-field, is not well understood. This feature has been ascribed to the existence of grain boundaries in YBCO films [40]. (e) FFT spectrum of the plain oscillations. Red, orange and green lines on the FFT graph correspond to h/e , $h/2e$ and $h/4e$ domains, respectively. A FFT peak at 22 (1/T) corresponds to the SC loop with 241 nm diameter, which is fairly close to the AFM extracted average loop diameter of 230 nm.

¹⁵ ΔT_{cmax} is obtained using approximation formula (8) and $\Delta T_{ctheory}$ using expression $\frac{\Delta T_{ctheory}}{T_c} = 0.14\xi_0^2/r^2$.

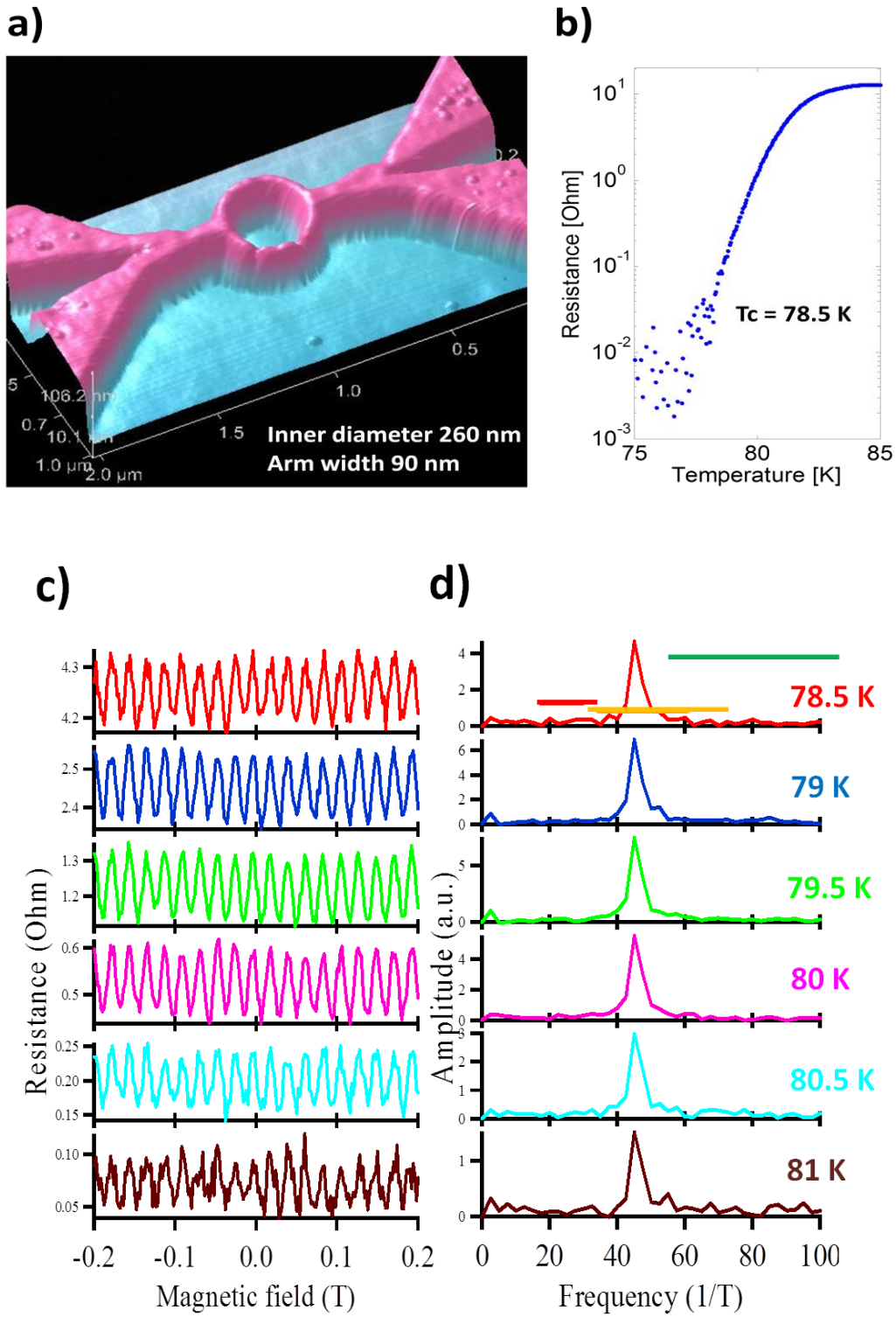


Figure 4.3: Ring on the optimally doped 30 nm 001-oriented YBCO on 110-cut MgO (film #2).

(a) AFM picture (inner diameter 260 nm; arm width 90 nm; average roughness ~ 1 nm, corresponding to one YBCO unit cell). (b) The corresponding resistive transition of the ring ($T_c \sim 78.5$ K). (c) Resistance oscillations in the (-0.2 – 0.2) T field range without subtracting the parabolic fit ($\Delta T_{cmax} \sim 80$ mK $\gg \Delta T_{ctheory} \sim 1$ mK). (d) FFT spectrum of the oscillations in the narrow field range: (-0.1 – 0.1) T. Red, orange and green lines on the FFT graph correspond to h/e , $h/2e$ and $h/4e$ domains, respectively. A FFT peak at 46 (1/T) corresponds to the SC loop with 350 nm average diameter, which coincides with the AFM extracted average loop diameter.

Chapter 5

Conclusions and future outlook

In this thesis work we have developed a PLD procedure for deposition of thin c -axis oriented YBCO films on LAO (001) substrates with different superconducting properties. The procedure allows for reproducible T_c vs. post-annealing pressure characteristics in the underdoped part of the SC dome down to 58 K. Submicron size nanorings were patterned on the optimally doped films and Little Parks oscillations identifying Cooper pairs as charge carriers detected.

Continuation of this work could follow two trajectories – one moving along the line of the UD part of the superconducting dome and the other one covering the remaining, overdoped, part.

Our UD stopping point of 58 K should be breached, given that the most exotic phenomena are expected to be observed in the highly UD regime. It is our belief that the particle-like features on our surfaces are preventing us from detecting the SC state below this point on the dome. Growth conditions for obtaining defect-free surfaces (which are also necessary for nanoscale device patterning) need to be optimized. A few attempts proved the deposition temperature to be the key parameter in tuning the surface properties. This would allow for investigation of the LP effect in this regime and possible verification of predicted h/e and $h/4e$ flux periodicities. Some improvement in the surface appearance has already been made on optimal YBCO grown on LAO by decreasing the deposition temperature to 780 °C. Furthermore, the task of optimizing the growth of UD c -axis YBCO films on LSAT and MgO in a reproducible manner could be undertaken, followed by the same fabrication and measurement procedure performed on films deposited on LAO. By doing this, one could attribute the possibly observed h/e and $h/4e$ oscillations to the low oxygen level in YBCO rather than to some substrate induced effect.

To complete the story related to doping dependence of SC properties, an entire SC dome should be covered. By ex-situ ozone treatment of the optimally doped YBCO films one reaches the overdoped regime. The work on this has already been started in our group and the first results are encouraging. The films obtained on MgO (110) show a drop in T_c compared to the optimal ones, while the XRD $2\theta - \omega$ scan displays a peak shift to the right, corresponding to the shrinkage of the YBCO cell in c -direction which is a signature of a higher oxygen concentration in YBCO. Ultimately, devices would be patterned on these films as well, and MR measurements performed, in order to learn more about superconducting mechanism in this doping regime.

Appendix A - XRD

XRD has become one of the most common characterization techniques for investigating crystallographic structure of materials. Many applications, ranging from analyzing substrate materials, layered structures, thin films, interfaces, determination of composition and thickness measurements, have made it an irreplaceable tool in studies on structural properties of materials.

XRD is based on Bragg's diffraction (figure A.1). The incoming X-ray beam hits the electrons in the atoms of the crystal lattice. The electrons become the sources of secondary spherical waves. These waves get annihilated in most directions through destructive interference. However, if the scattering centers (scatterers) are located periodically in planes equidistantly separated by a distance d , the waves originating from the scatterers will constructively interfere only if their path difference, $2d\sin\theta$, equals the multiple number of incoming beam wavelengths λ : $2d\sin\theta = n\lambda$ (Bragg's law). Only at the angles obeying the Bragg's law, the incoming rays get deflected from the surface and form a reflection spot in the diffraction pattern.

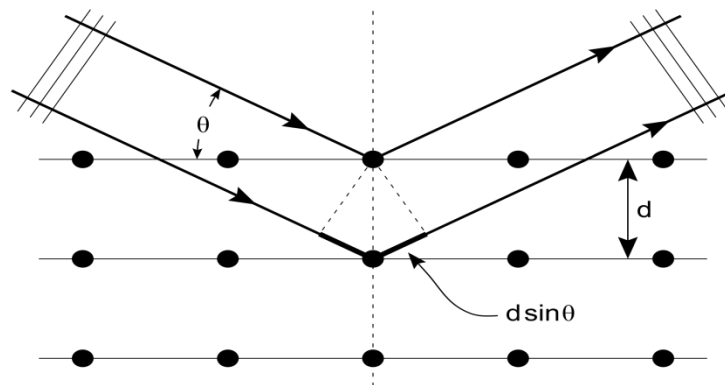


Figure A.1: Bragg's diffraction.

The three main parts of the X-ray diffractometer are the source of the X rays, the specimen on which the incoming X rays get scattered and the detector of the scattered X rays (figure A.2). There are several XRD measurements done for different purposes. For the film characterizations done in this thesis, two are relevant: $\omega - 2\theta$ scan (also denoted as $\theta - 2\theta$) and ω scan (also denoted as the rocking curve measurement). The $\omega - 2\theta$ scan provides out-of-plane information about the crystal lattice. Here, it was used to determine the lattice parameter of the YBCO unit cell in the growth direction of the film (perpendicular to the substrate). In this kind of the scan, the angle $2\theta = 2\omega$ is kept constant by changing simultaneously the ω and 2θ angles. The ω scan provides information about the film quality. The full width half maximum (FWHM) of the diffraction peak is inversely proportional to the dislocation density in the film. Here, only the 2θ angle is kept constant while ω is changed constantly throughout the scan.

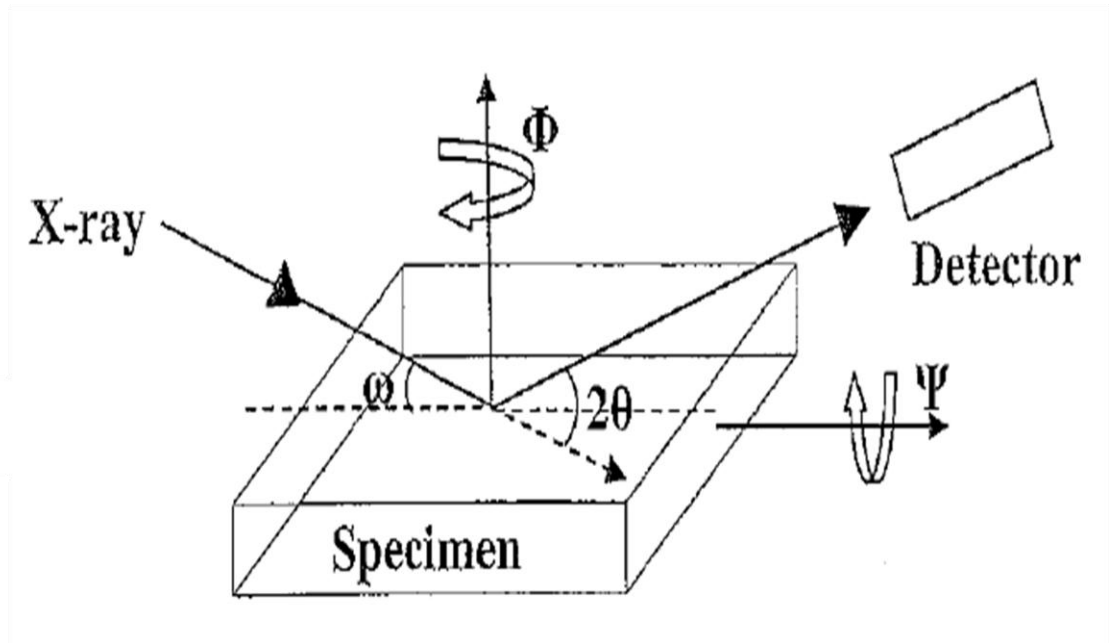


Figure A.2: XRD measurement set-up with the important angles: ω – the angle between the incoming X-ray beam direction and the specimen surface; 2θ – the angle between the incoming X-ray beam direction and the scattered X-ray beam direction.

Appendix B - PPMS

Electrical characterization of the films was done with PPMS. This system was designed to measure film sheet resistance at a range of temperatures and magnetic fields. The main part of the system is the PPMS probe, a tube containing the high-vacuum sample chamber and control systems of temperature and magnetic field. The sample is glued on a sample holder (puck) and connected with the circuit with gold wires. The puck is put into the bottom of the probe where it reaches an electrical connector. In this system, the problem of thermal gradients is avoided by pumping helium and nitrogen into an annular region surrounding the sample chamber, disabling direct contact of the sample with the gases. Cooling annulus is equipped with thermometers (figure B.1).

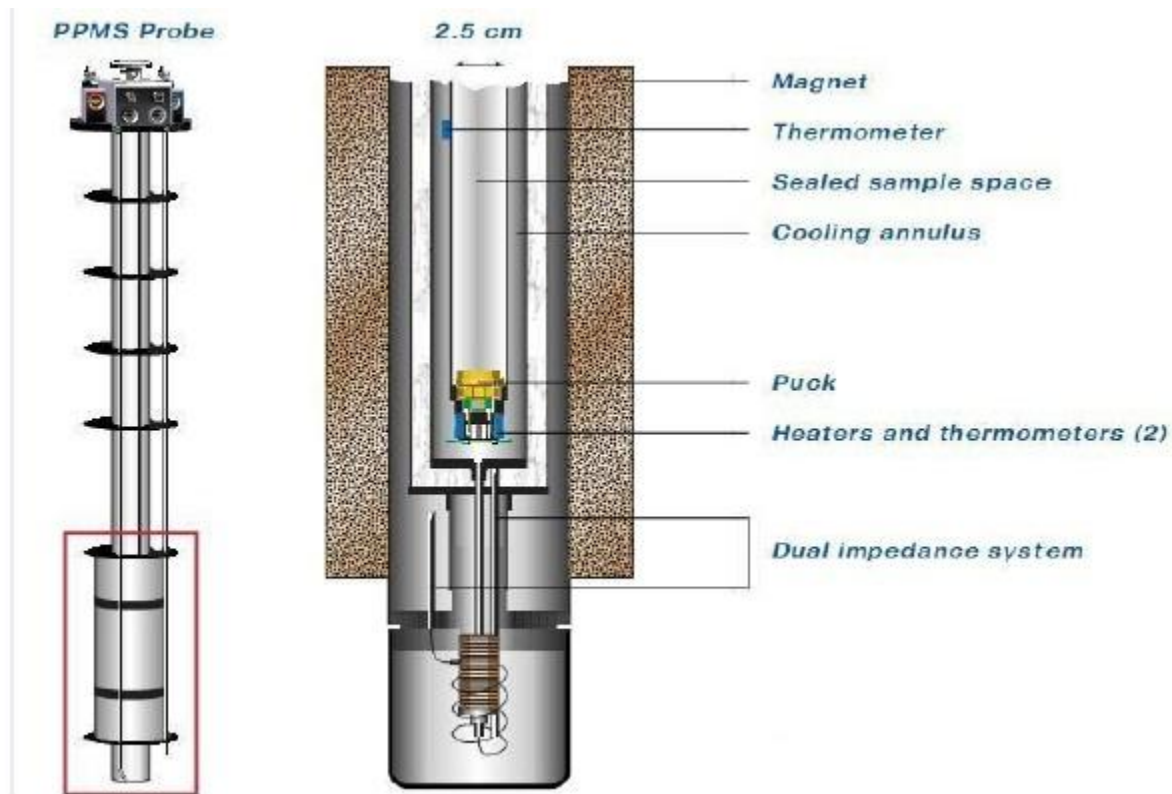


Figure B.1: Scheme of the PPMS system.

For films deposited for the purpose of this thesis, PPMS has been used to obtain their resistive transition curves. Resistance measurements were done using a four point probe method (figure B.2). The sample is connected to the measurement circuit through two current probes (used to run the current through the sample) and two voltage probes (used to measure the voltage drop over the sample). However, each of these four probes has three intrinsic resistances of its own that need to be taken into account. First, the probe has its own resistance (R_p). Furthermore, the physical contact of the probe with the sample gives rise to the probe contact resistance (R_{cp}). Finally, the current spreads into the film from the tip of the probe, creating the spread resistance (R_{sp}). The four probe measurement eliminates the problem of the current probes' stray resistances and to a large extent of the voltage ones as well. The reason for the last one lies in the high impedance of the voltmeter that makes the voltage drops over the voltage probe stray resistances very small (figure B.3). Hence, the voltmeter reading is very close to the real voltage drop over the sample.

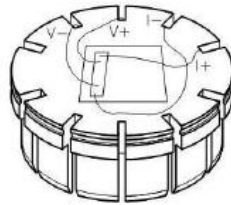


Figure B.2: Sketch of the four probe measurement set-up on a sample mounted on a PPMS puck.

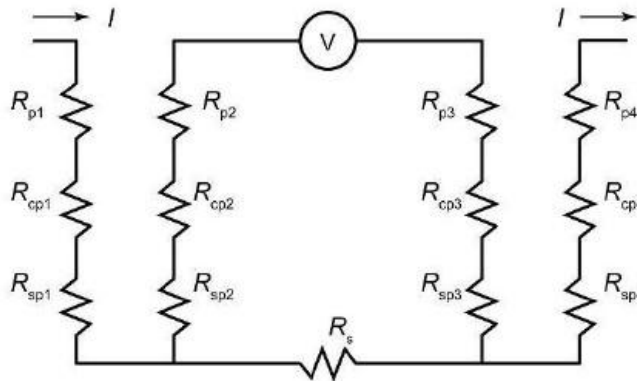


Figure B.3: Equivalent circuit for four point probe measurement of the film resistance. Indexes 1 and 4 correspond to the current probes, and 2 and 3 to the voltage ones.

Acknowledgements

My ‘thanks’ goes to:

...my supervisor, Prof. Floriana Lombardi, for being convincing in persuading me to join her group and invoking interest in me for this field of science; for the highly valuable guidance throughout the work that followed; for somewhat ‘unconventional’, but rather appreciable direct approach in communication

...my daily supervisor, Riccardo Arpaia, for all the early mornings, long days and late nights in the cleanroom and the lab; for the endless patience tested many times by numerous questions coming from my side during so many discussions; for being very successful in pedagogically approaching to me

...Prof. Thilo Bauch, for introducing me to this group; for helping Floriana and Riccardo with reading and correcting this report

...Sophie Charpentier, for all the help with the measurements

...Reza Baghdadi, for my very first days in the cleanroom

...Marco Arzeo, for the help with the simulation and the mask design parts

...the entire group for a warm welcome; for all the kindness throughout this period; for making the time spent working on this thesis not only beneficial, but also enjoyable

...MC2 for providing an amazing work environment

...Prof. Frederik Denef, for the enthusiasm with which he accepted to be a co-promoter of this thesis and the support along the way

...my EMM Nano coordinators for the enormous help in crucial moments

...my family and everyone else whose acts caused me making a step towards the point of writing this last line

Bibliography

- [1] J. G. Bednorz and K. A. Müller, "Possible high T_c superconductivity in the Ba-La-Cu-O system", *Z. Phys. B* 64, p. 189, 1986.
- [2] C. C. Tsuei and J. R. Kirtley, "Pairing symmetry in cuprate superconductors", *Rev. Mod. Phys.*, 72, p. 969, 2000.
- [3] V. Harlingen, "Phase-sensitive tests of the symmetry of the pairing state in the high-temperature superconductors-Evidence for $d_{x^2-y^2}$ symmetry", *Rev. Mod. Phys.*, 67, p. 515, 1995.
- [4] J. R. Kirtley, et. al., "Angle-resolved phase-sensitive determination of in-plane gap symmetry in YBCO", *Nature Physics*, 2, p. 190, 2006.
- [5] L. H. Greene, M. Covington, M. Aprili, E. Badica and D. E. Pugel, "Observation of broken time-reversal symmetry with Andreev bound state tunneling spectroscopy", *Physica B*, 280, p. 159, 2000.
- [6] G. Elhalel, R. Beck, G. Leibovitch and G. Deutscher, "Transition from a Mixed to a Pure d-Wave Symmetry in Superconducting Optimally Doped $\text{YBa}_2\text{Cu}_3\text{O}_{7-x}$ Thin Films Under Applied Fields", *Phys. Rev. Lett.*, 98, p. 137002, 2007.
- [7] M. Covington, et.al., "Observation of Surface-Induced Broken Time-Reversal Symmetry in $\text{YBa}_2\text{Cu}_3\text{O}_7$ Tunnel Junctions", *Phys. rev. Lett.*, 79, p. 277, 1997.
- [8] J. Bardeen, N. Cooper and J. R. Schrieffer, "Theory of superconductivity", *Phys. Rev.*, 108, p. 1175, 1957.
- [9] P. Monthoux, D. Pines and G. G. Lonzarich, "Superconductivity without phonons", *Nature*, p. 1177, 2007.
- [10] T. Timusk and B. Statt, "The pseudogap in high-temperature superconductors: an experimental survey", *Rep. Prog. Phys.*, 62, p. 61, 1999.

- [11] D. N. Basov and T. Timusk, "Electrodynamics of high- T_c superconductors", *Rev. Mod. Phys.*, *77*, p. 721, 2005.
- [12] M. Tinkham, Introduction to superconductivity, New York: McGraw-Hill, 1996.
- [13] W. A. Little and R. D. Parks, "Observation of quantum periodicity in the transition temperature of a superconducting cylinder", *Phys. Rev. Lett.*, *9*, pp. 9-12, 1962.
- [14] R. D. Parks and W. A. Little, "Fluxoid quantization in a multiply-connected superconductor", *Phys. Rev. A* *133*, pp. 97-103, 1964.
- [15] V. Juricic, I. F. Herbut and Z. Tesanovic, "Restoration of the magnetic hc/e -periodicity in unconventional superconductors", *Phys. Rev. Lett.* *100*, p. 187006, 2008.
- [16] F. Loder et. al., "Magnetic flux periodicity of h/e in superconducting loops", *Nature Phys.* *4*, pp. 112-115, 2008.
- [17] V. Vakaryuk, "Universal mechanism for breaking the $hc/2e$ periodicity of flux-induced oscillations in small superconducting rings", *Phys. Rev. Lett.* *101*, p. 167002, 2008.
- [18] T. C. Wei and P. M. Goldbart, "Emergence of h/e -period oscillations in the critical temperature of small superconducting rings threaded by magnetic flux", *Phys. Rev. B* *77*, p. 224512, 2008.
- [19] J. X. Zhu and H. T. Quan, "Magnetic flux periodicity in a hollow d-wave superconducting cylinder", *Phys. Rev. B* *81*, p. 054521, 2010.
- [20] E. Berg, E. Fradkin and S. A. Kivelson, "Charge- $4e$ superconductivity from pair-density-wave order in certain high-temperature superconductors", *Nature Phys.* *5*, pp. 830-833, 2009.
- [21] F. Carillo et. al., "Little-Parks effect in single nanoscale $YBa_2Cu_3O_{6+x}$ rings", *Phys. Rev. B* *81*, p. 054505, 2010.
- [22] R. Arpaia, S. Nawaz, F. Lombardi and T. Bauch, "Improved Nanopatterning for YBCO Nanowires Approaching the Depairing Current", *IEEE Trans. Appl. Supercond.* *23*, p. 3, 2013.
- [23] W. Pickett, "Electronic structure of the high-temperature oxide superconductors", *Rev. Mod. Phys.*, *61*, p. 433, 1989.

- [24] R. Cava, "Oxide superconductors", *J. Am. Ceram. Soc.* 83, pp. 5-28, 2000.
- [25] David Gustafsson, "Nanoscale $\text{YBa}_2\text{Cu}_3\text{O}_{7-\delta}$ devices - Searching for a subdominant order parameter using a single electron transistor", Chalmers - MC2, Gothenburg, 2012.
- [26] D. Reznik, J.-P. Ismer, I. Eremin, L. Pintschovius, T. Wolf, M. Arai, Y. Endoh, T. Masui, and S. Tajima, "Local-moment fluctuations in the optimally doped high- T_c superconductor $\text{YBa}_2\text{Cu}_3\text{O}_{6.95}$ ", *Phys. Rev. B* 78, p. 132503, 2008.
- [27] C. C. Homes, S. V. Dordevic, D. A. Bonn, R. Liang, W. N. Hardy and T. Timusk, "Coherence, incoherence, and scaling along the c axis of $\text{YBa}_2\text{Cu}_3\text{O}_{6+x}$ ", *Phys. Rev. B*, 71, p. 184515, 2005.
- [28] D. N. Zheng, A. M. Campbell, J. D. Johnson, J. R. Cooper, F. J. Blunt, A. Porch and P. A. Freeman, "Magnetic susceptibilities, critical fields, and critical currents of Co- and Zn-doped $\text{YBa}_2\text{Cu}_3\text{O}_7$ ", *Phys. rev. B.*, 49, p. 1417, 1994.
- [29] M. K. Wu, et. al., "Superconductivity at 93 K in a New Mixed-Phase Y-Ba-Cu-O Compound System at Ambient Pressure", *Phys. Rev. Lett.*, 58, p. 908, 1987.
- [30] D. Gustafsson, D. Golubev, M. Fogelström, T. Claeson, S. Kubatkin, T. Bauch and F. Lombardi, "Fully gapped superconductivity in a nanometre-size $\text{YBa}_2\text{Cu}_3\text{O}_{7-\delta}$ island enhanced by a magnetic field," *Nature Nanotechnology Letters*, 2012.
- [31] P. Bernstein, J. F. Hamet and Y. Thimont, "Transport properties of $\text{YBa}_2\text{Cu}_3\text{O}_{7-\delta}$ thin films near the critical state with no applied magnetic field", *Physica C* 468, p. 200, 2008.
- [32] Z. X. Ye, Q. Li, Y. Hu, W. D. Si, P. D. Johnson and Y. Zhu, "Enhanced Flux Pinning in $\text{YBa}_2\text{Cu}_3\text{O}_{7-\delta}$ Films by Nano-scaled Substrate Surface Roughness", *Appl. Phys. Lett.* 87, p. 122502, 2005.
- [33] A. Lukashenko, A. V. Ustinov, A. P. Zhuravel, E. Hollman and R. Wördenweber, "Laser scanning microscopy of guided vortex flow in microstructured high- T_c films", *J. Appl. Phys.* 100, p. 023913, 2006.
- [34] S. A. Hayward, S. A. T. Redfern and E. K. H. Salje, "Order parameter saturation in LaAlO_3 ", *J. Phys.: Condens. Matter* 14, p. 10131, 2002.

- [35] S. Bueble, K. Knorr, E. Brecht and W. W. Schmahl, "Influence of the ferroelastic twin domain structure on the {100} surface morphology of LaAlO₃ HTSC substrates", *Surf. Sci.* 400, p. 345, 1998.
- [36] S. Nawaz, "Approaching the depairing critical current in superconducting YBa₂Cu₃O_{7-x} nanowires", Chalmers - MC2, Gothenburg, 2013.
- [37] P. L. Gammel, P. A. Polakos, C. E. Rice, L. R. Harriott and D. J. Bishop, "Little-Parks oscillations of T_c in patterned microstructures of the oxide superconductor YBa₂Cu₃O₇: Experimental limits on fractional-statistics-particle theories", *Phys. Rev. B* 41, p. 2593, 1990.
- [38] R. P. Groff and R. D. Parks, "Fluxoid Quantization and Field-Induced Depairing in a Hollow Superconducting Microcylinder", *Phys. Rev.* 176, p. 567, 1968.
- [39] D. Y. Vodolazov, D. S. Golubovic, F. M. Peeters, and V. V. Moshchalkov, "Enhancement and decrease of critical current due to suppression of superconductivity by a magnetic field", *Phys. Rev. B* 76, p. 134505, 2007.
- [40] D. Levi, A. Shaulov, A. Frydman, G. Koren, B. Ya. Shapiro and Y. Yeshurun, "Periodic negative magnetoresistance in granular YBa₂Cu₃O_{7-δ} nanowires", *EPL* 101, p. 67005, 2013.
- [41] B. P. Martins, *Recent Developments in Superconductivity Research*, New York: Nova Science, 2006.
- [42] V. S. Boyko, "Dislocation description of twins in high-temperature superconductor YBa₂Cu₃O_{7-δ}", *Low Temp. Phys.* 34, p. 503, 2008.